Precambrian Research 254 (2014) 226–244

Contents lists available at ScienceDirect

Precambrian Research

journal homepage: www.elsevier.com/locate/precamres

Is the Precambrian basement of the Tarim Craton in NW China composed of discrete terranes?

Chuan-Lin Zhang[a,*], Hai-Bo Zou[b], M. Santosh[c], Xian-Tao Ye[a], Huai-Kun Li[d]

[a] Nanjing Institute of Geology and Mineral Resources, CGS, Nanjing 210016, China
[b] Department of Geology and Geography, Auburn University, Auburn 36849-5305, USA
[c] School of Earth Sciences and Resources, China University of Geosciences Beijing, 29 Xueyuan Road, Beijing 100083, China
[d] Tianjin Institute of Geology and Mineral Resources, Tianjin 300170, China

ARTICLE INFO

Article history:
Received 17 April 2014
Received in revised form 21 August 2014
Accepted 22 August 2014
Available online 6 September 2014

Keywords:
Tarim Craton
Early Precambrian evolution
Zircon U–Pb geochronology
Hf isotope composition
Continental growth

ABSTRACT

The Precambrian evolution of the Tarim Craton in NE China, in particular during the early Precambrian stage, remains enigmatic. In this contribution, we report field observation, petrology, geochemistry, zircon Lu–Hf isotopes and U–Pb ages of the major rock formations of the Aketage area in the southeastern section of the Tarim Craton. The Milan Group in Aketage is dominantly composed of 2.7–2.5 Ga gneissic amphibolite–TTG complex with minor paragneiss. Both the mafic and silicic rocks exhibit geochemical features consistent with an arc affinity. The arc-signature of the 2.01–2.03 Ga gneissic granites and gabbros which intrude the Archean basement, as well as the major 2.0 Ga metamorphic event revealed by zircon U–Pb dating, suggest an important subduction-collision event possibly related to the assembly of the Paleoproterozoic Columbia supercontinent. The ca. 1848–1856 Ma massive potassic granites, 1867 Ma mafic dyke swarm and 1844 Ma massive leucogranite dykes reveal magmatism in a post-collisional extensional setting.

A comprehensive synthesis of the major orogenic events and continental crust growth process from the different Precambrian terranes in Tarim Craton show significant discrepancy in time related to the late Neoarchean crust formation ages and the Paleoproterozoic orogenic events. For example, the major orogenic event took place at ~1.85 Ga in Quruqtagh-Dunhuang terrane, at ~1.90 Ga in the southwest Tarim Craton and at ~2.0 Ga in the Aketage-Qaidam terrane. These different terranes exhibit distinct periods of continental crust growth in the early Precambrian. Continental growth in the Aketage area took place during 2.7–4.3 Ga. The 3.6 Ga xenocrystic zircons as well as the peak of 4.2 Ga zircon Hf model ages, indicate the possible existence of Paleoarchean and even Hadean crust in the Aketage area. In the Quruqtagh-Dunhuang terrane, the growth of early Precambrian continental crust took place at 2.6–3.3 Ga with peaks at ca. 2.6–2.7 Ga and 3.0 Ga. The diachronous late Paleoproterozoic orogenic events and the significant difference in continental growth process suggest that the Precambrian basement of the Tarim Craton is composed by independent continental terranes possibly detached from the cores of discrete ancient cratonic nuclei, which were not unified until the early Neoproterozoic during assembly of the Rodinia supercontinent.

1. Introduction

The Tarim Craton, located within the Xinjiang Uygur Autonomous Region of northwestern China and covering an area of more than 600,000 km^2, is one of the main three Precambrian nuclei in China (i.e., Tarim, North China and South China) (Zheng et al., 2013). The Tarim Craton is surrounded by the orogenic belts of Tienshan Mountains to the north, the western Kunlun Mountains to the south, and the Central-Southern Altyn Tagh Mountains to the southeast (Fig. 1a). Since most part of the Tarim Craton is covered by aeolian sands and also because of the difficulties in accessibility, the Precambrian basement of Tarim Craton remains obscure.

In recent years, many studies focusing on the Neoproterozoic geology of Tarim Craton revealed that the craton was assembled within the Rodinia supercontinent during 1.0–0.9 Ga, and even lasted to 780 Ma (Zhang et al., 2003, 2012a, 2014; Shu et al., 2011; He et al., 2013; Yong et al., 2013). The two main pulses of Neoproterozoic magmatism at 820–800 Ma and 780–760 Ma have been correlated to the Rodinian plume activity (Zhang et al., 2007a, 2009,

* Corresponding author. Tel.: +86 25 84897863; fax: +86 25 84600446.
E-mail address: zchuanlin1968@gmail.com (C.-L. Zhang).

http://dx.doi.org/10.1016/j.precamres.2014.08.006
0301-9268/

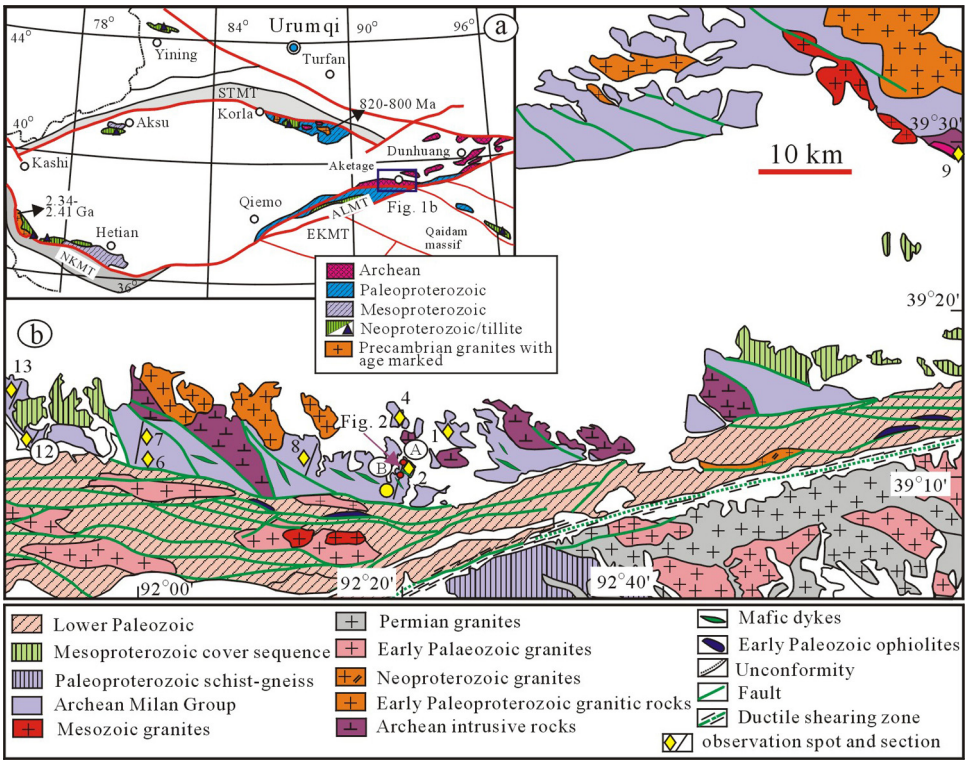

Fig. 1. (a) Tectonic framework of the Tarim Craton and its marginal area showing the Precambrian terranes along its margin. (b) Precambrian geology in Aketage area in the eastern section of the Tarim Craton. The field observation spots and sections are shown and the number beside the diamond symbol shows our sampling locality and correspond with the sample numbers in the text and Supplementary Table S1.

2012a; Xu et al., 2005, 2009). The limited geochronological data for the early Precambrian history of this craton shows 2.0–1.80 Ga metamorphism along the northern margin (the Quruqtagh uplift), the Tiekelike uplift in southwest and the Altyn in the east, all of which have been correlated to the assembly of the Columbia supercontinent (Lu et al., 2008; Shu et al., 2011; Long et al., 2010, 2011a,b; Zhang et al., 2011; He et al., 2013). However, a number of questions remain to be addressed such as: (1) When did the Tarim Craton acquire a unified Precambrian basement? (2) Did the different Precambrian terranes around the Tarim Craton (Fig. 1a) experience similar Precambrian tectonic evolution? (3) Do these Precambrian terranes share a common continental crust growth process?

With a view to obtain a better understanding of the early Precambrian evolution and continental crust growth in the Tarim Craton, we report new geological, geochronological and geochemical data from the early Precambrian rocks in Aketage area along the southeastern margin of the craton. Based on the results from this study and previous data, we investigate the processes and timing of cratonization in Tarim and their correlation with the assembly and breakup of early Precambrian supercontinents.

2. Regional geology and field observations

The early Precambrian rocks in Tarim Craton are mostly exposed along the eastern and northern margins of the craton (Fig. 1a). These major rock types include Neoarchean tonalitic–granitic units, and the Paleoproterozoic amphibolite to granulite facies paragneiss (Lu, 1992; Lu et al., 2002; Lu and Yuan, 2003; Zhang et al., 2013a). The Neoarchean gneissic granitoids in Quruqtagh can be divided into three groups: the TTG (tonalite, trondhjemite, granodiorite as well as gabbro enclaves), calc-alkaline granites and high Ba–Sr granites. Recent high-precision zircon U–Pb ages indicate that the TTG rocks were mainly emplaced at ca. 2.7–2.6 Ga and that these were intruded by the 2.53 Ga high Ba–Sr granites (Zhang et al., 2012b).

Similar to the scenario in the Quruqtagh, previous studies have classified the early Precambrian lithounits in Altyn-Tagh and Dunhuang area as Archean Milan Group and Paleoproterozoic Altyn Mountain Group based on limited imprecise isotope ages (e.g., Xinjiang BGMR, 1993; Lu et al., 2002). In recent years, geological mapping, geochronological and geochemical studies revealed that the Milan Group is composed of Archean TTG rocks (2.7–2.6 Ga) (Lu et al., 2008; Liu et al., 2010), hypersthene granulite, and mafic granulite (Lu et al., 2008). The supracrustal sequences are represented by aluminous metapelites and minor graphite-bearing marble, similar to the 'khondalite series' in the North China Craton. They are also comparable with the paragneiss from Quruqtagh in their similar petrographic features (Lu et al., 2002, 2008).

This study focuses on the Early Precambrian units in Aketage area immediately to the north of Altyn-Tagh (Fig. 1b), where the oldest xenocrystal zircons in Tarim were reported (~3.6 Ga, Lu et al., 2008). Our field observations show that the Milan Group in this area is mainly composed of silicic orthogneiss with minor amphibolites (grey gneiss) and paragneiss (Figs. 2 and 3a–c). These gneisses are intruded by diverse magmatic rocks including gneissic granites, massive granites and mafic dykes (Figs. 2 and 3d–h). In several places, the massive granites, mafic dykes and some leucogranite dykes intrude into the gneissic granites and the gneisses of Milan Group (Fig. 3b and e–h). Generally, amphibolite enclaves occur within the felsic gneiss and both of these share concurrent gneissic structure (Fig. 3c), indicating that they underwent a similar deformation history before the intrusion of the mafic dykes and massive granites. Based on field observations, we divide the igneous activities in the Aketage area into an early stage of the gneissic granites and gabbros, and a late stage of the massive granites and mafic dykes (Fig. 2).

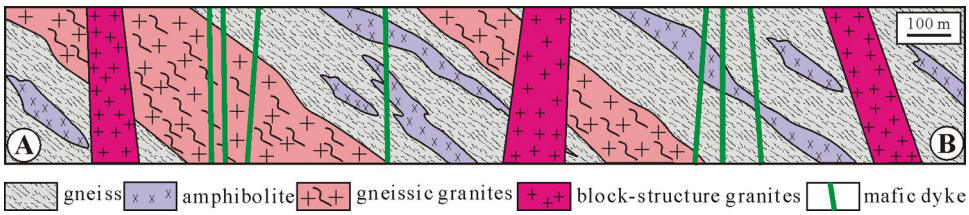

Fig. 2. Typical geological section along the Aketage showing three main phases of igneous activities revealed by the field relationship between the Archean amphibolite-gneiss, gneissic granites, massive granite and mafic dyke swarm (see detailed description in the text).

2.1. The grey gneisses

Amphibolites from the Milan Group are medium- to coarse-grained and comprise mainly plagioclase (50–60%), hornblende (30–40%), biotite (2–5%), and minor pyroxene (1–5%) with occasional quartz (Fig. 3i). Apatite and Ti–Fe oxide occur as accessory minerals. Based on the mineral assemblage, we infer that their protoliths were most likely mafic igneous rocks (basalt or gabbro). The gneisses from the Milan Group include biotite plagioclase gneiss, amphibole (pyroxene)-bearing plagioclase gneiss and biotite schist containing variable modal content of biotite (5–30%), amphibole (2–15%), quartz (15–35%), and plagioclase (10–40%). According to the mineral assemblage and texture, most of the amphibole (pyroxene)-bearing gneisses are tonalitic–trondhjemitic rocks (Fig. 3j–k). Nevertheless, the minor biotite quartz schists might have been derived from sedimentary protoliths despite the absence of highly aluminous minerals in these rocks (Fig. 3l).

2.2. The gneissic granites and gabbros

The gneissic granitoids intruding into the Milan gneisses are trondhjemites or tonalites exhibiting medium to coarse-grained texture. The dominant minerals are plagioclase (35–55%, including some zoned oligoclase), microperthitic microcline (10–30%), green-brown biotite (1–2%), hornblende (5–15%), quartz (25–35%), Ti–Fe oxide (2–5%) and accessory minerals such as allanite, titanite, apatite and zircon.

The gabbroic intrusion is exposed at the western-most part of the Aketage region (Fig. 1b). It shows sharp contact but shows foliation concordant with the structure of the host gneisses. The dominant minerals in the metagabbro are plagioclase (40–60%) and clinopyroxene (30–40%) with minor oxides. In thin sections, minor phlogopite is occasionally seen, possibly related to hydrothermal alteration. Some clinopyroxene occurs as phenocryst (Fig. 3m).

2.3. The massive granites and mafic dykes

The massive potassic granite plutons show intrusive contact with the Milan gneisses as well as the gneissic trondhjemite and tonalite plutons (Fig. 2). They display medium to coarse granitic texture with dominant primary minerals including microperthitic microcline (30–35%), orthoclase (20–25%), quartz (40–45%), biotite (2–5%) and accessory minerals composed of zircon, titanite, and apatite. No primary aluminous minerals such as cordierite or garnet are observed (Fig. 3n).

The mafic dykes are mainly diabase and diabasic gabbro. Fine-grained gabbroic rocks are seen at the center of some of the thick dykes (>3 m). The diabase shows xenomorphic mafic minerals and Ti–Fe oxide filling the spaces between the sub-euhedral plagioclase (Fig. 3o). Gabbros are mainly composed of plagioclase (40–50%), clinopyroxene (30–45%), hornblende (2–5%), Ti–Fe oxides (1–10%) and minor olivine (less than 1%). Olivine occurs as inclusions in clinopyroxene. Some of the hornblende grains are primary with subhedral crystal forms and are partly replaced by actinolite and biotite in some thin sections.

3. Sample preparation and analytical procedures

In this study, 14 samples were selected for zircon U–Pb geochronology and Hf isotope analysis. Fifty-five whole-rock samples were collected from different rock types for geochemistry. The rock types and co-ordinates of their locations are given in Supplementary Table S1.

Inline Supplementary Table S1 can be found online at http://dx.doi.org/10.1016/j.precamres.2014.08.006.

Zircon separation was carried out using conventional magnetic and density techniques to concentrate non-magnetic, heavy fractions. Zircon grains were then hand-picked under a binocular microscope. The grains and zircon standard 91500 were mounted in epoxy mounts that were then polished to section the crystals in half for analysis. All zircons were documented with transmitted and reflected light micrographs as well as cathodoluminescence (CL) images to reveal their internal structures. Zircon ages and Hf isotope compositions were analyzed using the LA-ICPMS method at Tianjin Institute of Geology and Mineral Resources, Chinese Geology Survey (CGS). The detailed analytical procedures are the same as those described in Hou et al. (2009) and Geng et al. (2011). The Hf isotope measurements were performed mostly on the ablated spots where U–Pb analysis was made. Softwares SQUID 1.0 and ISOPLOT (Ludwig, 1999, 2001) were used for zircon U–Pb data processing. The weighted mean ages are quoted at 95% confidence level. Zircon U–Pb and Hf isotope data are presented in Supplementary Tables S2 and S3, respectively.

Inline Supplementary Tables S2 and S3 can be found online at http://dx.doi.org/10.1016/j.precamres.2014.08.006.

Major and trace element concentrations were measured at the Guangzhou Institute of Geochemistry, Chinese Academy of Sciences. Major elements were analyzed using a Rigaku ZSX100e XRF following the analytical procedures described by Li et al. (2004). Analytical precision is generally better than 2%. Trace elements were analyzed using a Perkin-Elmer Sciex ELAN 6000 ICP-MS following procedures described by Li et al. (2004). An internal standard solution containing single element Rh was used to monitor signal drift during ion counting. The USGS standards BCR-1, W-2, and G-2, and the Chinese National standards GSR-1 and GSR-3, were used for calibrating element concentrations of measured samples. In-run analytical precision for most elements was generally better than 2–5%. The analytical results are presented in Supplementary Table S4.

Inline Supplementary Table S4 can be found online at http://dx.doi.org/10.1016/j.precamres.2014.08.006.

4. Zircon geochronology

4.1. Ages of the gneisses from the Milan Group

The zircons from samples AYT01, AYT02 and AYT09.1 have very similar features. Most grains from these three samples are anhedral, up to 100–250 μm in length, and have aspect (length/width) ratios of 1:1 to 3:1. Most of the zircons are transparent and colourless to slight pinkish. In CL images, core-mantle structure is commonly

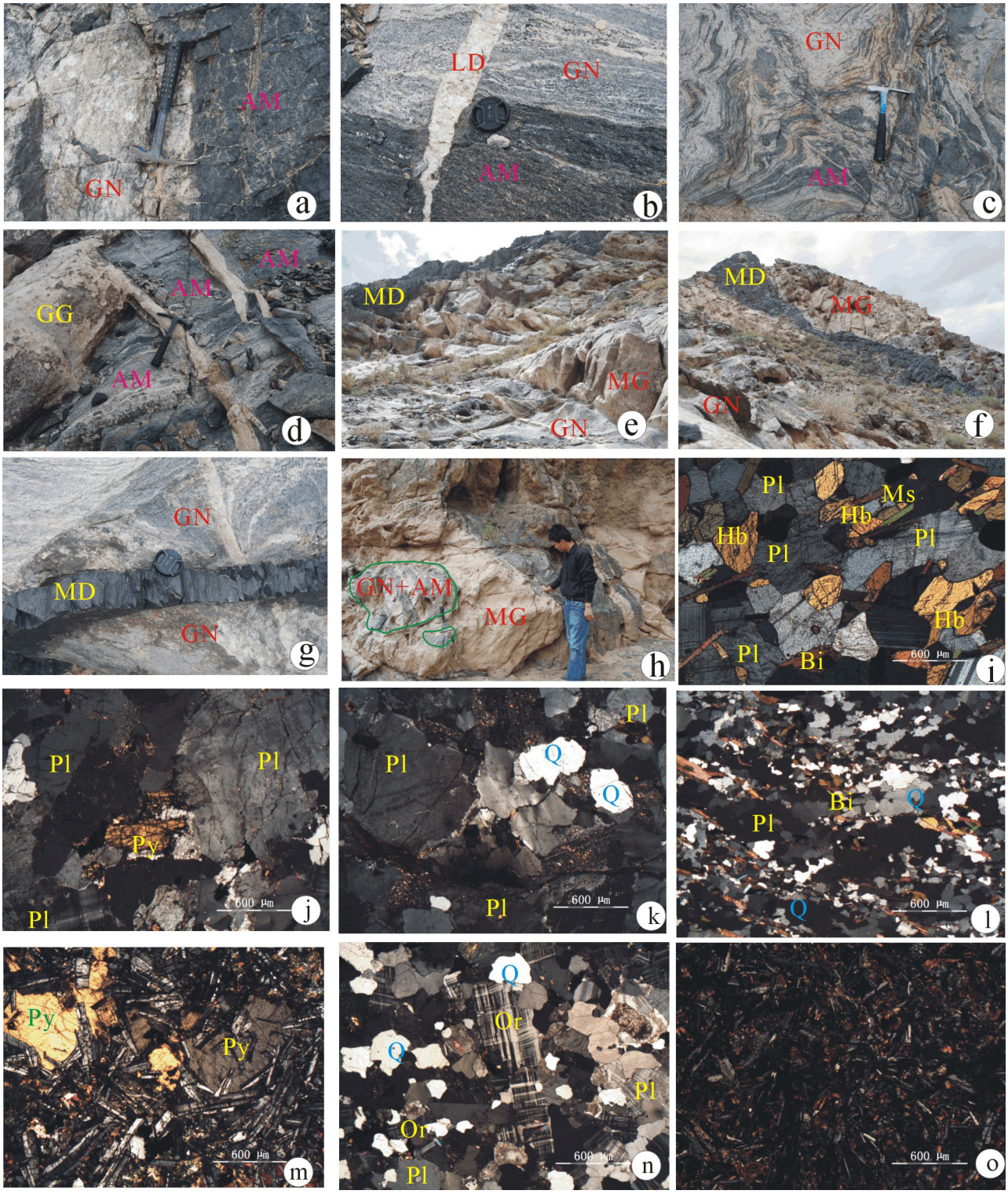

Fig. 3. Representative field photos and photomicrographs showing the Precambrian rocks in Aketage. (a–c) Intermingling between the amphibolite and TTG gneiss. (d–e) Archean gneisses intruded by massive granites and mafic dykes. (f) Mafic dyke sharp intrusive contact with the Archean gneiss. (g) Gneissic granites intruding into the Archean granitic gneiss. (h) Massive potassic granites intruding into the Archean amphibolite-gneiss with amphibolite-gneiss occurring as xenoliths in the massive potassic granites. (i and j) Archean gneiss with magmatic protoliths (k) Amphibolite showing their magmatic texture. (l) Biotite quartz schist occurring within gneisses. (m) Gneissic gabbro, showing clinopyroxene phenocryst. (n) Massive potassic granites showing twinning of the microcline phenocryst. (o) Diabase showing typical ophitic texture. GN, gneiss; GG, gneissic granite; MG, massive granite; MD, mafic dyke; AM, gneissic amphibolite; Pl, plagioclase; Py, clinopyroxene; Bi, biotite; Hb, hornblende; Q, quartz.

seen in most of the zircon grains. The cores are CL dark whereas the overgrowth mantles are brighter (Fig. 4). According to their inner structure, anhedral form, melting corrosion and relatively dark CL character, we deduce that the cores were of igneous origin. The bright mantle is clearly of metamorphic origin. Some zircon grains from the sample AYT02 are generally CL bright, lacking core-mantle structure or significant zoning. These features indicate their metamorphic origin (Finch and Hanchar, 2003)

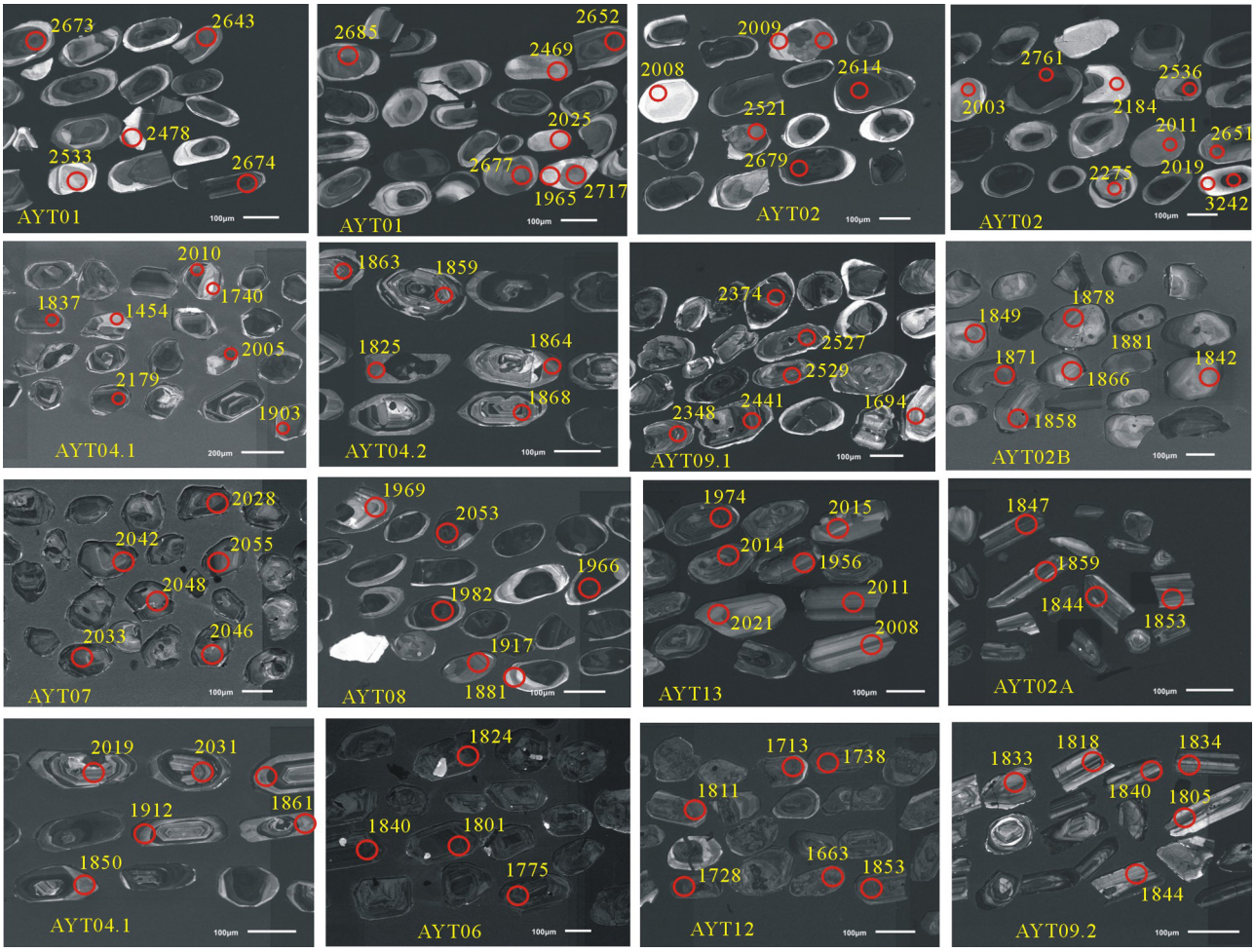

Fig. 4. CL images of representative zircons. Analytical spots and ages in Ma are shown (see detailed discussions in the text).

(Fig. 4). Thirty-seven analysis (on 35 zircons) and 54 analyses (on 50 zircons) were conducted for sample AYT01 and AYT02, respectively (Supplementary Table S2). Most analyses on zircons from sample AYT01 yield concordant $^{206}Pb/^{238}U$ and $^{207}Pb/^{235}U$ ages, and among these (Fig. 5a), eighteen analyses on the cores yield concordant and consistent older ages with a weighted mean $^{207}Pb/^{206}Pb$ age of 2674 ± 11 Ma (N = 18, MSWD = 1.6) (Fig. 5b). Six analyses on the overgrowth mantle and two on the metamorphic zircon grains (see Fig. 4) yield relatively younger but consistent $^{207}Pb/^{206}Pb$ ages with a weighted mean value of 2490 ± 19 Ma (N = 8, MSWD = 1.4) with low U contents (U = 13–73 ppm) and high Th/U ratios (0.4–1.87, mostly above 1.0). These eight analyses define an upper intercept age of 2508 ± 30 Ma on the Concordia diagram (N = 8, MSWD = 1.03) (Fig. 5a) and display radiogenic lead loss. Five analyses on the metamorphic zircons show markedly lower abundance of U and Th (9–46 ppm and 9–36 ppm respectively) with Th/U ratios of 0.3–1.8. Nevertheless, these five analyse yield consistent ages within analytical error with a weighted $^{206}Pb/^{238}U$ mean age of 2006 ± 28 Ma (N = 5, MSWD = 0.5) (Fig. 5a). The data suggest that the granitic gneiss crystallized at 2674 ± 11 Ma and underwent two phases of metamorphism at ~2.5 Ga and 2.0 Ga, respectively. Generally, metamorphic zircons have low Th/U ratios (<0.1). However, several studies indicate that the Th/U ratios of metamorphic zircons are constrained by multiple factors, e.g., the crystal growth rate, presence of fluids, among other factors. Zircons which crystallized rapidly in a relatively short time might possess high Th/U ratios up to 0.7 (Vavra et al., 1999; White and Kamber, 2002) and some zircons that crystallized under high-pressure and high-temperature metamorphic process possess Th/U ratios higher than 3.0 (Santosh et al., 2009).

The results of the 54 analyses conducted on 50 zircons of the sample AYT02 are shown in Fig. 5c (also see Supplementary Table S2). Among these, about 10% of the analyzed spots exhibit variable radiogenic lead loss and they deviate from the Concordia line (Fig. 5c). However, the analyses on the cores yield older ages varying from 2746 Ma to >2400 Ma, indicative of their detrital origin. Zircons with $^{207}Pb/^{206}Pb$ ages younger than 2.5 Ga plot below the concordant curve except for spot 21, indicating variable radiogenic lead loss. Thus, we speculate that the sedimentation age of this paragneiss was no later than 2.5 Ga. Fifteen analyses on the overgrowth mantle domains and on the zircons with bright CL properties yield concordant and consistent ages, with weighted $^{206}Pb/^{238}U$ age of 1999 ± 16 Ma (MSWD = 0.43) (Fig. 5c).

Most zircons from sample AYT09.1 are euhedral, up to 200 μm in length, and have aspect ratios of 1:1 to 2:1. All zircons are transparent colourless with a few showing slightly pinkish colour. Euhedral concentric zoning is common in most crystals. Some zircon grains have thin (mostly less than 10 μm) and bright overgrowth rims and no significant inherited cores have been observed in CL images (Fig. 4). Thirty analyses on 30 zircon grains were obtained (Supplementary Table S2). Three spots on rounded zircon rimmed by bright mantle yield older ages ($^{207}Pb/^{206}Pb$ age = 2.62–2.85 Ga), indicating that these zircons are inherited grains (Fig. 4). Five spots yield relatively juvenile ages with variable radiogenic lead loss, and in combination with their Th/U ratios (0.08–0.12), we suggest that they were formed during subsequent metamorphism. The other 22 analyses

锆石的结晶速度快以及在高压下形成的锆石以及遭受高温高压变质的锆石都具有**high Th/U**比

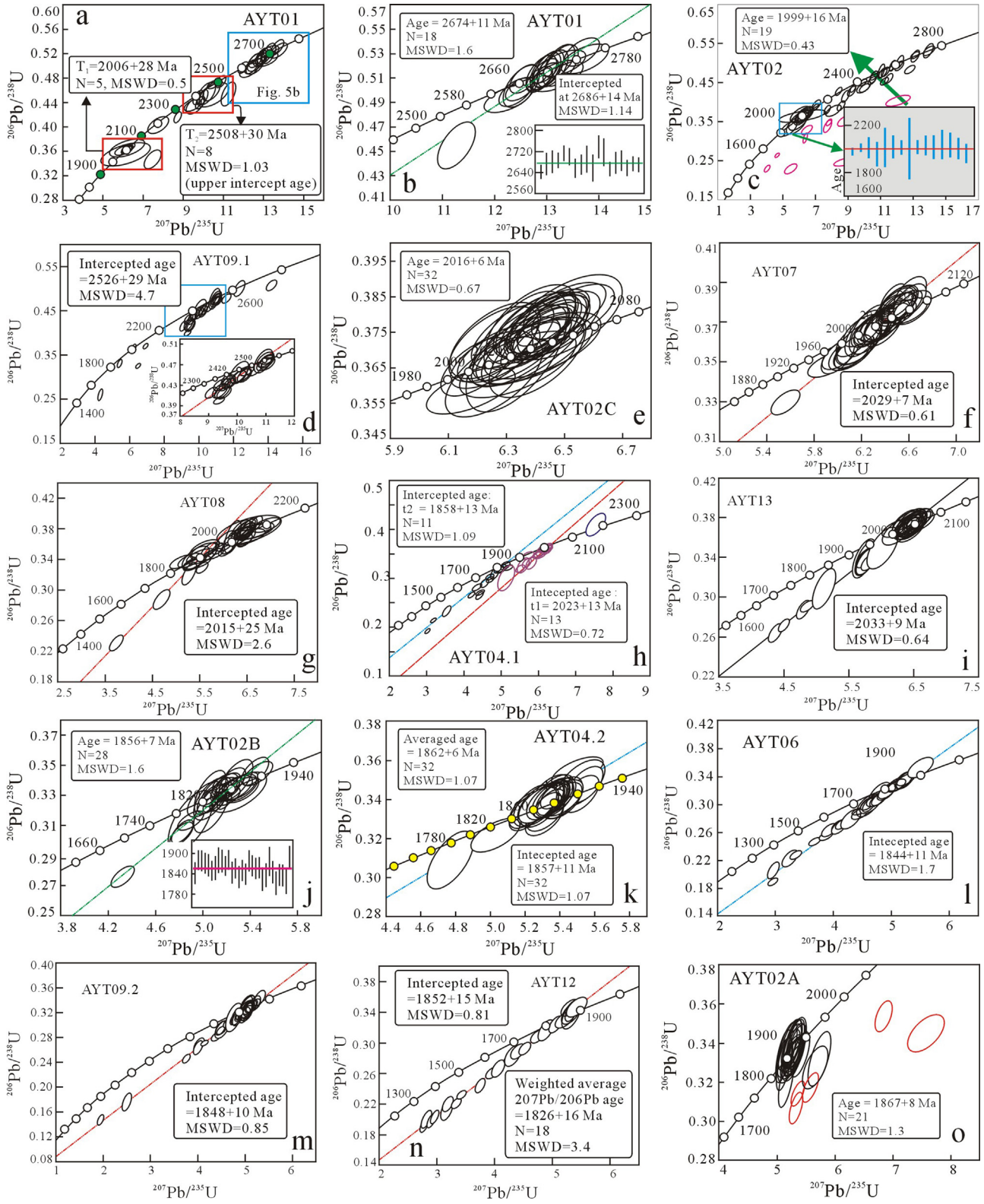

Fig. 5. Concordia plots of U–Pb zircon data for zircons from the Archean gneiss and schist, Paleoproterozoic gabbro, gneiss granite, massive granites and mafic dykes (see text for detailed description).

on the euhedral columnar grains with clear zoning have variable U and Th contents with Th/U ratios ranging from 0.2–1.0. Although some of these exhibit slight radiogenic lead loss, they define a clear discordant line with upper intercept age of 2526 ± 29 Ma (Fig. 5d) (MSWD = 4.7). This age is interpreted as the best estimation of the crystallization age of the granitic protolith of the gneiss.

4.2. Ages of the gneissic granites and gabbros

Most of the zircon grains from sample AYT02C and AYT07 are subhedral and have dimensions ranging from 100 to 150 μm with aspect ratios of 1–2 (Fig. 4). Most grains show no significant zoning and no core-mantle structure under CL. Thirty-two and thirty

analyses were conducted in zircons from sample AYT02 C and AYT007, respectively. The results show variable U and Th contents with Th/U ratios ranging from 0.3 to 0.8 (Supplementary Table S2). The total 32 analyses of sample AYT02C show concordant $^{206}Pb/^{238}U$ and $^{207}Pb/^{235}U$ ages within analytical errors and yield a weighted mean $^{206}Pb/^{238}U$ age of 2016 ± 6 Ma (MSWD = 0.67) (Fig. 5e). The data from sample AYT07 show variable radiogenic lead loss but all the analyses define a discordia with an upper intercept age of 2029 ± 7 Ma (MSWD = 0.61) (Fig. 5f). Moreover, the $^{207}Pb/^{206}Pb$ ages are consistent within error and yield a weighted mean age of 2026 ± 6 Ma (MSWD = 3.0), comparable with the upper intercept age.

Thirty-seven analyses on zircon grains from sample AYT08 have variable U and Th contents with Th/U ratios of 0.1–0.7. Most analyses yield concordant but inconsistent ages varying from 1.9 Ga to 2.1 Ga. Among them, several spots on the overgrowth mantles yield relative younger ages (Fig. 4), possibly representing metamorphic event. Thirty-five analyses define a discordant line with upper intercept age of 2015 ± 25 Ma (MSWD = 2.6) (Fig. 5g), and this age is interpreted to represent the crystallization age of gneissic granite

Zircons from sample AYT04.1 are euhedral to subhedral and up to 200 μm in length with aspect ratios of 1–2. Some zircons have very thin overgrowth rim and some show heterogeneous convoluted texture similar to some of the zircons reported from granulite facies rocks (Fig. 4, Hoskin and Schaltegger, 2001). Thirty-two analyses were conducted on 31 zircons and most analyses exhibit variable radiogenic lead loss. One spot (spot 14) yields older $^{206}Pb/^{238}U$ age of 2218 Ma, likely to be of inherited origin. Several analyses are excluded because of their significant discordance. The remaining 24 analyses could be divided into two sub-groups. Group I defines a clear discordia with upper intercept age of 2023 ± 13 Ma (MSWD = 0.72) (Fig. 5h) and group II defines a discordant line with upper intercept age of 1858 ± 11 Ma (MSWD = 1.09) (Fig. 5h). Taking into account the field observation and the results from other samples, we suggest that the older age (2023 Ma) represents the crystallization age of the gneissic granite and the younger age (1858 Ma) represents a subsequent tectonothermal event.

Zircons from the metagabbro sample AYT13 are euhedral to subhedral, up to 200–300 μm in length, and have aspect ratios of 2:1 to 4:1 (Fig. 4). Thirty-two analyses on 32 zircon grains were obtained (Supplementary Table S2), and the results show variable U and Th contents with Th/U ratios between 0.03 and 1.1 (most above 0.2 with three spots having Th/U ratios less than 0.1). Among the 32 analyses, eleven show variable degrees of radiogenic lead loss and the others yield consistent and concordant $^{206}Pb/^{238}U$ and $^{207}Pb/^{235}U$ ages. However, in the concordia diagram, the 32 analyses define a clear discordia with an upper intercept age of 2033 ± 9 Ma (MSWD = 0.64) (Fig. 5i).

4.3. Ages of the massive granites, lecuogranite dykes and mafic dykes

Although zircons from the massive granites and lecuogranite dykes (sample AYT02B, AYT04.2, AYT06, AYT09.2 and AYT12) display variable forms, length, aspect ratios and CL images (Fig. 4), all the grains display igneous crystallization features. The analytical results listed in Supplementary Table S2 show that zircons in some of the samples underwent variable radiogenic lead loss. Nevertheless, these five samples yield consistent concordant or upper intercepted ages at ca. 1.85 Ga (Fig. 5j–n), indicating nearly coeval emplacement of the massive granites and silicic lecuogranite dykes.

Zircon grains from the mafic dykes (sample AYT02A) show features typical of zircons crystallized in mafic intrusions (Fig. 4) with banded structure and with length ranging from 80 μm to 150 μm and aspect ratios of 2–4. Among the thirty analyses conducted for this sample (Supplementary Table S2), six spots show variable radiogenic lead loss. Two grains yield older ages and they are likely to be xenocrysts. The other 22 analyses have consistent and concordant ages within analytical errors and yield a weighted mean age of 1867 ± 8 Ma (MSWD = 1.3) (Fig. 5o), and this age is interpreted to represent the emplacement age of the mafic dykes.

5. Geochemistry

5.1. The Achaean amphibolites and the granitic gneisses

The amphibolites and the granitic gneisses have SiO_2 contents ranging from 46.8% to 53.6% and from 58% to 75%, respectively. In the Harker diagram, the amphibolites and the granitic gneisses show consistent correlation (Fig. 6), with decreasing CaO, Fe_2O_3, MgO and TiO_2 and increasing Na_2O, K_2O and Zr against SiO_2. However, Al_2O_3 shows increase for the amphibolites but it shows decrease for the granitic gneisses.

Most amphibolite samples are sub-alkaline in character and display tholeiitic feature with respect to their major element and HFSE compositions (Fig. 7a and b). The granitic gneisses display a large range of SiO_2 contents as well as other major elements (Supplementary Table S3). They plot in the trondhjemite to tonalite field in An–Ab–Or triangle (Fig. 7c).

The amphibolites have variable total REE contents ranging from 42 ppm to 290 ppm and they show consistent distribution patterns with enrichment in LREE without significant or moderate negative Eu anomalies (δEu = 0.8–1.0) normalized to the Chondrite (both the Chondrite and the Primitive Mantle are after Sun and McDonough, 1989) (Fig. 8a). Their incompatible elements in spider diagram exhibit systematic depletion in Nb–Ta and enrichment in LILEs. Negative to positive anomalies of Sr, P and Ti are also observed (Fig. 8b). The granitic gneisses have total REE ranging from 36 ppm to 255 ppm and show significant LREE-enriched distribution patterns with marked negative through negligible to positive Eu anomalies (Fig. 8c). On the primitive mantle normalized spider diagram, all the samples show consistent Nb–Ta trough and most samples have variable depletion in P and Ti (Fig. 8d).

5.2. The gneissic granites and gabbros

The gneissic granites have consistent major element compositions except for one diorite sample which has the lowest SiO_2 (61%) and K_2O (3.86%) (Supplementary Table S4). All the samples have comparable Na_2O and K_2O contents and their total alkali ranges from 7.9% to 8.5%. On the Harker diagram, Al_2O_3, CaO, Fe_2O_3, MgO, TiO_2, and Sr decrease with increasing SiO_2, but Na_2O, K_2O and Zr show no significant correlation with SiO_2 contents (Fig. 6). Based on CIPW norms, the rocks plot in the quartz monzonite field of An-Ab–Or triangle (Fig. 7c). The gneissic granites have total REE contents ranging from 196 ppm to 476 ppm (mostly less than 300 ppm) and they show consistent REE patterns with significant enrichment of LREE ($(La/Yb)_N$ = 49–253, mostly above 100) and insignificant Eu anomalies (Fig. 8e). As for incompatible elements, they show variable enrichment of LILEs (Rb, Ba, Sr) and depletion of HFSEs. Importantly, there is a significant depletion in Nb–Ta and P relative to neighbouring elements (Fig. 8f). Two samples of the 2033 Ma gneissic gabbro show major and trace element compositions similar to those of the amphibolites (Supplementary Table S2). Their REE and incompatible element distribution patterns exhibit significant arc signatures (Fig. 8a and b).

5.3. The mafic dykes

The mafic dykes have restricted major elements contents (Supplementary Table S4) except for two wall-rock contaminated samples (sample AYT04H5, AYT04H6). On Harker diagrams, Sr, Zr,

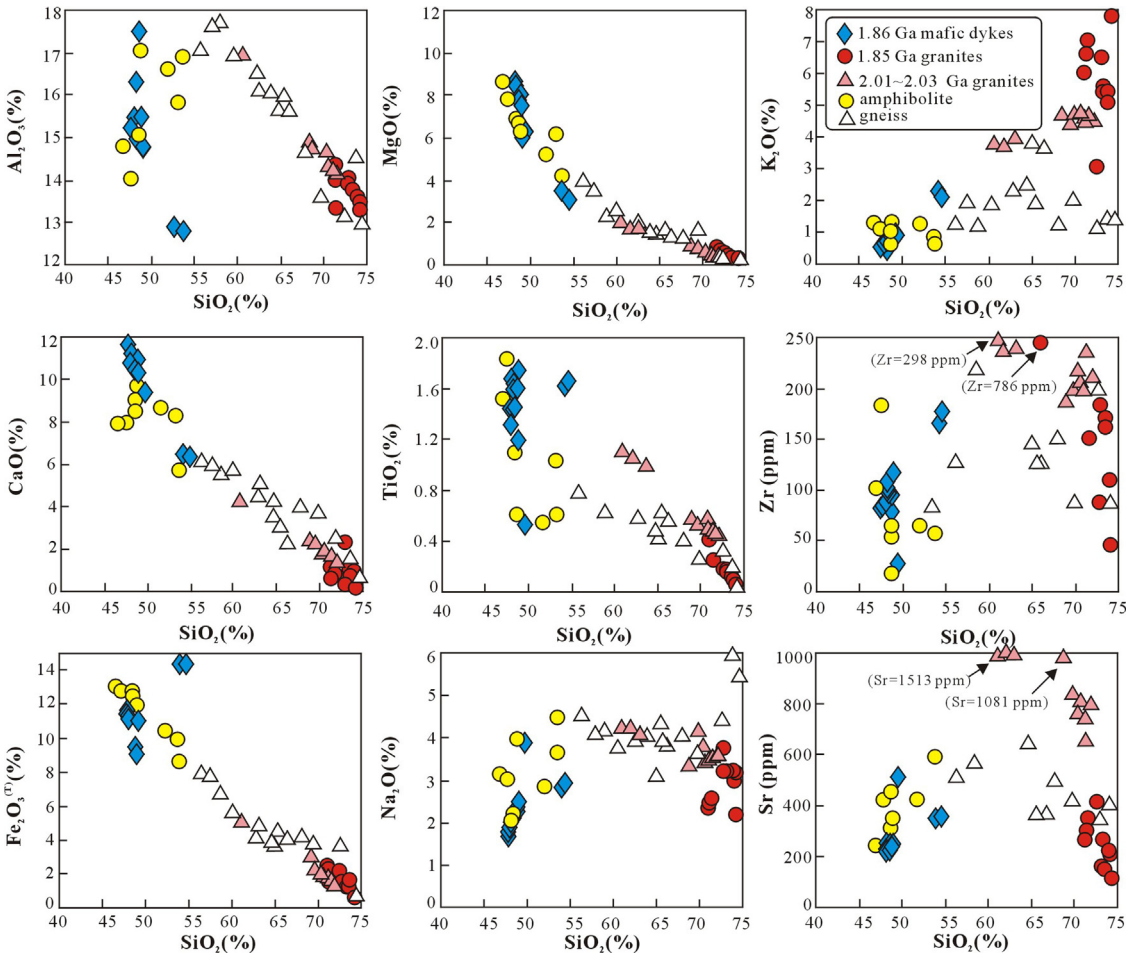

Fig. 6. Classification diagrams for the Archean amphibolite-gneiss, Paleoproterozoic gneissic granites, massive granites and mafic dykes (see details in the text).

K_2O and Na_2O increase and Al_2O_3, CaO and MgO decrease as SiO_2 increases (Fig. 6). The total alkali vs. SiO_2 diagram shows that the mafic dykes are sub-alkaline, which is consistent with their incompatible element classifications (Fig. 7b, after Winchester and Floyd, 1977). Their $Fe_2O_3^{(T)}$/MgO ratios and TiO_2 contents show tholeiitic signatures.

5.4. The massive granites

The massive potassic granite samples have high SiO_2 (>70 wt.%), K_2O (5.3–7.8%) and total alkalis (8.4–10%), and low MgO (0.2–0.9 wt.%), Fe_2O_3 (0.7–2.5%), TiO_2 (0.05–0.44). Their major element characteristics indicate a peraluminous nature with A/CNK values of 1.03–1.07. According to their total alkali and SiO_2 contents, all the samples exhibit sub-alkaline features (Fig. 7a). They have a large range of total REE contents (39–3082 ppm) and are enriched in LREE relative to HREE with high $(La/Yb)_N$ ratios ranging from 33 to 668. One sample (AYT02-2) shows significant positive Eu anomaly (δEu = 12.6) and the other samples show positive to negative Eu anomalies (δEu = 1.7–0.4) (Fig. 8i). On the primitive mantle normalized trace element spider diagram, the rocks are enriched in LILE and depleted in Nb, Sr, P and Ti, leading to low Nb/La (0.01–0.3) (Fig. 8j).

6. Zircon Hf isotope compositions

Almost all the dated zircons were also measured for their Lu–Hf isotope compositions and the results are presented in Supplementary Table S3 (calculation formulae and the ages used in calculations are listed at the footnote of this table).

Based on the data, we divide all the samples into three groups. Group I, the early Paleoproterozoic to Achaean zircons, have $\varepsilon Hf(t)$ ranging from −11.2 to 5.48, and the oldest zircon from sample AYT02 has the highest $\varepsilon Hf(t)$ (Fig. 9). Group II, the 2000–2029 Ma zircons, exhibit large range of $\varepsilon Hf(t)$ values ranging from −16.76 to 2.87. Zircons from the gneissic gabbro sample AYT13 have the highest $\varepsilon Hf(t)$, ranging from −1.31 to 2.87 and most of them are positive. Group III, the 1826–1867 Ma zircons, have $\varepsilon Hf(t)$ varying from −12.1 to 3.0. The mafic dyke sample from this group has negative $\varepsilon Hf(t)$ between −8.9 and −4.3.

In the age vs. $\varepsilon Hf(t)$ diagram, their evolution trend significantly deviates from that of the Mesoarchean basement of the North China Craton and the Yangtze Craton. Among the three groups, Group I and Group III share similar crustal residence ages except the mafic dyke sample, and their T_{DM}^C mostly varies from 2.8 Ga to 3.8 Ga with peaks at 2.9 Ga, 3.3 Ga and 3.6 Ga. T_{DM}^C of the Group II zircons varies from 2.6 Ga to 4.3 Ga with peaks at 2.8 Ga, 3.1 Ga, 3.3 Ga and 4.2 Ga (Fig. 10).

7. Petrogenesis

7.1. The Neoarchean gneisses and amphibolites

The field relations showing the coeval nature of the amphibolite and granitoids (Fig. 3c), in combination with their geochemical features showing good correlation between SiO_2 and other oxides,

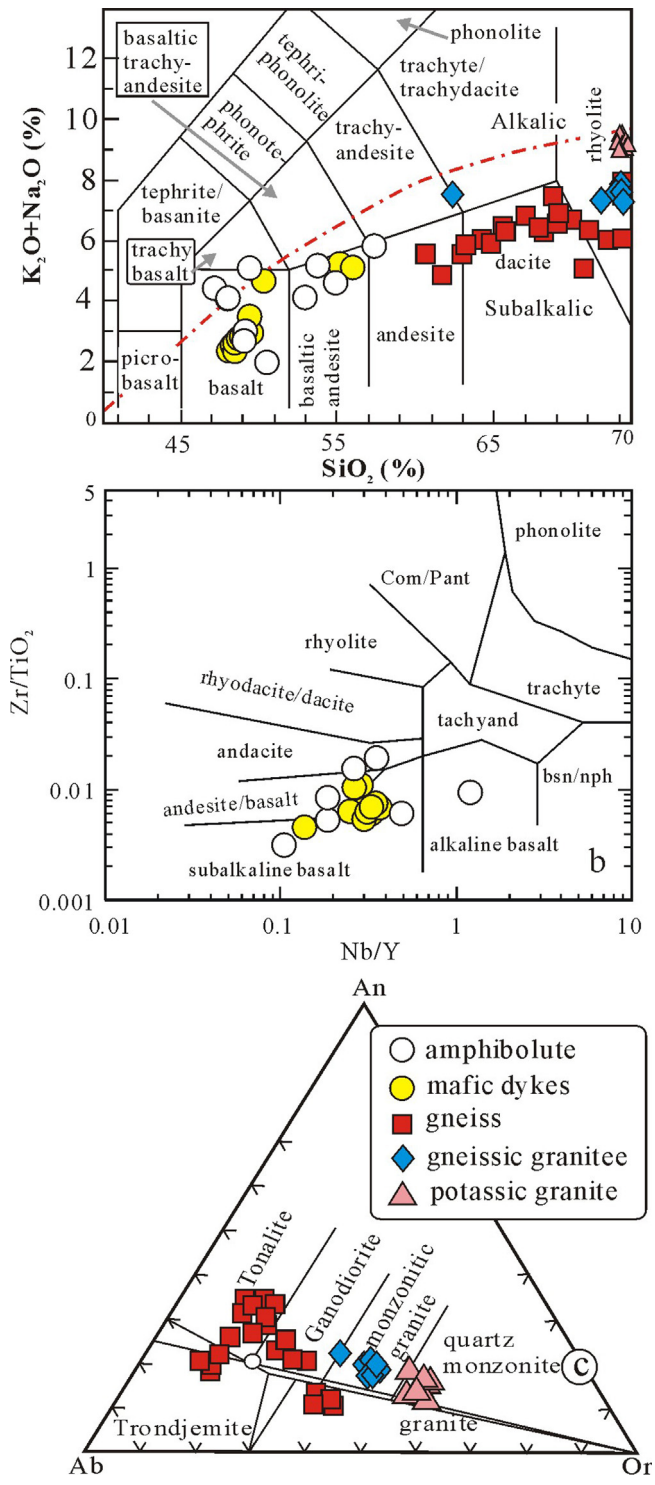

Fig. 7. Harker variation diagram for the Archean amphibolite-gneiss, Paleoproterozoic gneissic granites, massive granites and mafic dykes (SiO_2 vs. SiO_2, Na_2O, K_2O, TiO_2, $Fe_2O_3^T$, Al_2O_3, CaO, Cr, Zr and REE. Samples of the Archean amphibolite-gneiss and gneissic granites reported by Liu et al. are also included).

suggest that these rocks have a common petrogenetic history. The geochemical features of the gneisses and the absence of Al-rich minerals attest to their magmatic origin.

The amphibolites occurring within the granitic gneisses were derived from a mantle source as inferred from their low SiO_2 and high MgO contents. Their geochemical features are closely comparable with those of arc tholeiite (Fig. 11, Pearce and Cann, 1973; Pearce, 2008; Vermeesch, 2006), including the enrichment of LREE, LILE and depletion of HREE and HSFE, low TiO_2 (0.55–1.84%), P_2O_5 (0.11–0.35%), low Nb/Y (0.11–0.36), Nb/La (0.13–0.55), $Zr/P_2O_5 \times 10{,}000$ (0.07–0.1) and Ti/V (<25) ratios (Winchester and Floyd, 1976; Pearce and Cann, 1973; Pearce et al., 1992). Their chemical features suggest that the parent magma was derived from partial melting of a metasomatized sub-continental lithospheric mantle source (SCLM) or mantle-wedge source. In the incompatible elemental ratios (Fig. 12a–d), the amphibolites exhibit very different evolutionary trend with that of the 1857 Ma mafic dykes in this area (Fig. 12a–d) (see discussion below) but are similar to arc basalts. In addition, Nb/Th ratios show positive correlation with Nb/La (Fig. 12b) revealing variable crustal contamination which, in conjunction with field observations attest to intermingling between amphibolites and gneisses. Crustal contamination could elevate LILE, LREE relative to HFSE and HREE leading to low HFSE/LREE ratios (such as Nb/La) (Rudnick and Gao, 2003). However, since there is no correlation between Nb/La ratios with $Mg^{\#}$ (figure not shown), we argue that their low Nb/La ratios as well as their arc-signature in the incompatible element spider diagrams reflect their primitive magma feature, though the amphibolites incorporated variable proportion of crustal materials.

The gneisses coexisting with the garnet-free amphibolite could be directly derived from partial melting of the amphibolite similar with the scenario in high-temperature orogenic belts or magmatic arcs (Sawyer et al., 2010). Numerous studies have demonstrated that the trace element compositions of partial melts are different from that of the source because of the different partition coefficients of the trace elements in hornblende and plagioclase (Huang et al., 2012; Bagas et al., 2013; Lee and Cho, 2013). However, the amphibolite and the gneiss show similar total REE with no significant elevated LREE in the gneiss samples (Fig. 8c), indicating that the amphibolite and the gneiss were most likely derived from distinct magma sources.

Major elements of the granitic gneisses evolved from trondhjemite–tonalite through granodiorite to granite, similar to the trend of Archean TTGs. It is generally accepted that the geochemical features of TTG magmas originate from the partial melting of a mafic precursor although models on the processes involved in the petrogenesis of TTG rocks are equivocal (Martin, 1999; Martin and Moyen, 2003; Martin et al., 2005; Rudnick and Fountain, 1995; Condie, 2005; Kerrich and Polat, 2006; Smithies et al., 2003, 2005, 2007; Kemp and Hawkesworth, 2003; Whalen et al., 2002). Martin et al. (2005) suggested that adakitic magmas are the modern analogues of the Archean TTGs and that the close compositional similarities between high-SiO_2 adakites (HSA) and Late Archean TTGs (<~3.0 Ga) strongly suggest a petrogenetic analogy. In this study, we notice that the Archean gneisses could be divided into two groups according to their trace elemental signatures. Group I shows high Sr/Y and $(La/Yb)_N$ similar to those of the adakites and Group II has low Sr/Y and $(La/Yb)_N$ ratios and plots into the typical arc igneous rocks in Sr/Y vs. Y diagram (Fig. 13). According to their major and incompatible elements (Wang et al., 2006), Group I plots in the field of thickened lower crust-derived adakitic rocks and Group II deviates from the typical adakite fields of different origins (Fig. 14). Peacock et al. (1994) demonstrated that water-unsaturated (~5% H_2O) partial melting of mafic rocks produces a plagioclase-free residual assemblage containing garnet + amphibole. On the other hand, pressure is another important factor for formation of the Group I rocks. Numerous studies estimated that the crustal thickness required to generate 'slab-like' melts and garnet amphibole or eclogite residues within the lower crust is in the range from 27 km (Tate and Johnson, 2000) to >40 km (Wolde et al., 1996; Petford et al., 1996), with the lower end of the range involving wet melting of metabasaltic crust. Garnet, hornblende and rutile could be the main minerals in the residue, based

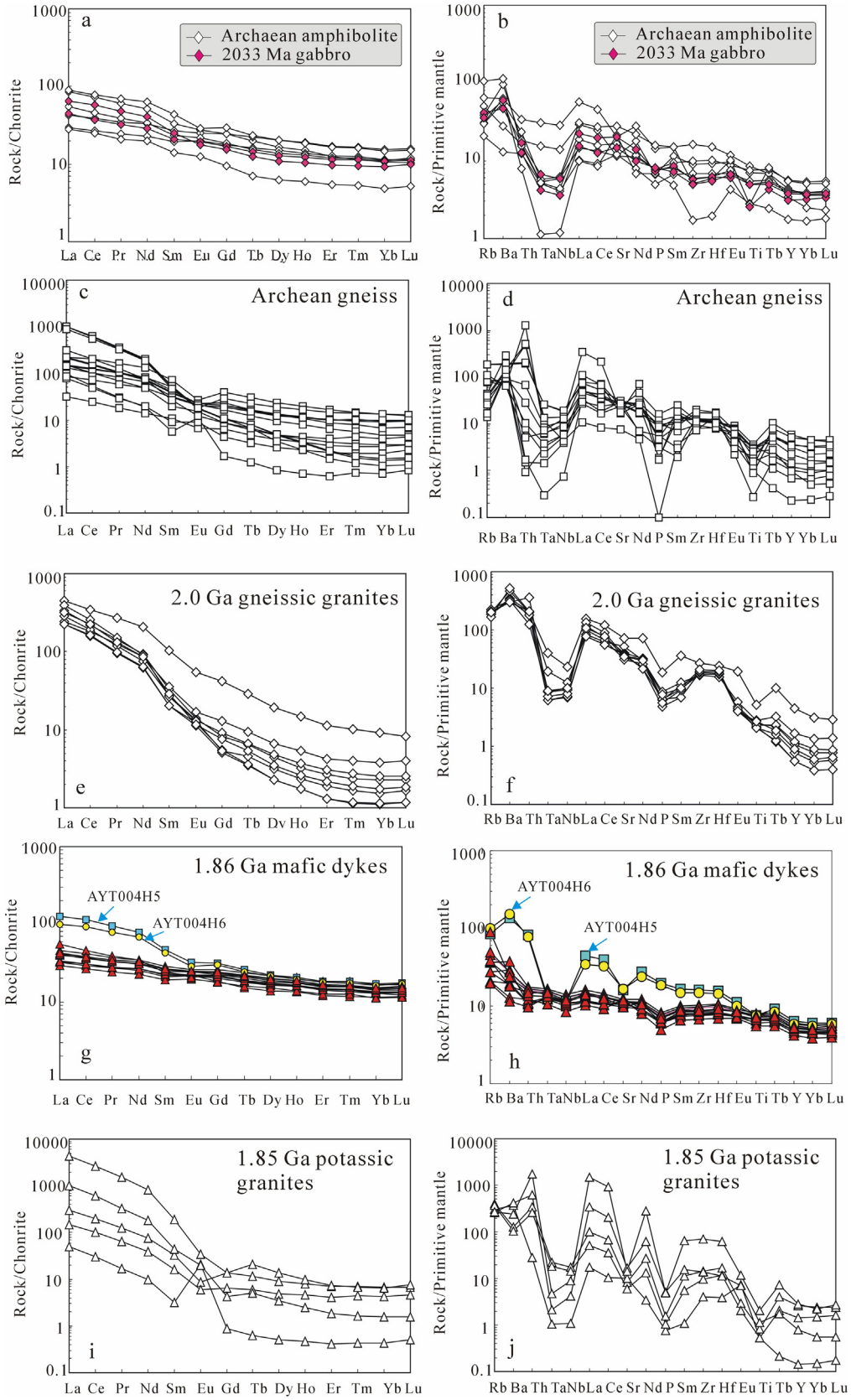

Fig. 8. Chondrite-normalized REE patterns and primitive mantle - normalized incompatible element spider diagrams for the studied rocks. The normalization values are from Sun and McDonough (1989) (see details in the text).

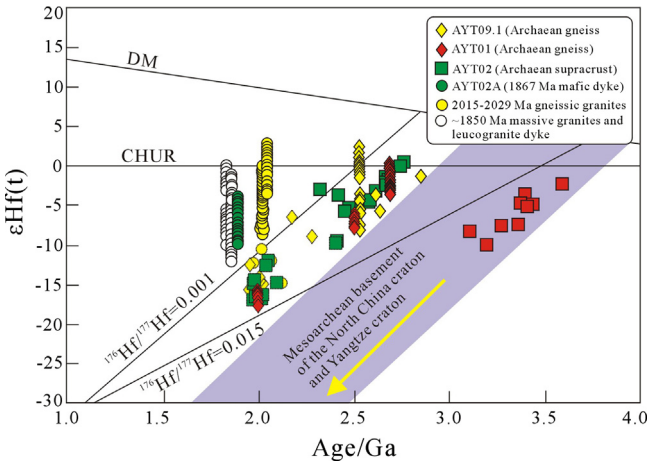

Fig. 9. Crystallization age vs. $\varepsilon Hf(t)$ diagram (the legend with dashed frame represents the metamorphic origin zircon. See details in the text).

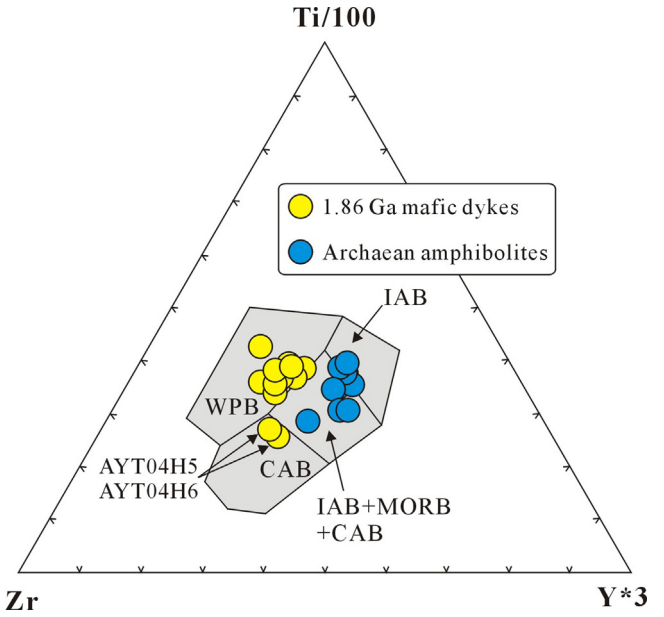

Fig. 11. Ti/100 – Zr – Y*3 triangle diagram showing the typical intraplate geochemical signatures of the Piqiang complex, the Bachu mafic dykes, and the basalts (after Pearce and Cann, 1973).

on their depletion in HREE and HFSE, and pronounced Ti negative anomalies on the trace element spider diagrams (Xiong et al., 2006). According to their high $(La/Yb)_N$ (19–28), Y/Yb ratios (12–14) and negligible Eu anomalies, garnet, rather than hornblende, could be the main mineral in the plagioclase-free residue (Stern and Kilian, 1996). In summary, we suggest that the adakite-like Group I rocks were derived from partial melting of a mafic precursor at a depth of >30 km with garnet and hornblende as the main residue.

Our field studies have revealed neosomes or leucosomes resulting from partial melting of the gneisses occurring as lenses and stripes (Fig. 3b and f), similar to the scenario in many Achaean metamorphic terranes (Lee and Cho, 2013 and references therein). These neosomes or leucosomes in the several gneiss samples (i.e., the Group II) might have contributed to the geochemical deviation of Group I rocks (Figs. 13 and 14), particularly the higher SiO_2 contents for the Group II rocks as compared with that of Group I. For the same reason, positive or negative Eu anomalies could be ascribed to cumulation of plagioclase or plagioclase left in the residue during partial melting process (Fig. 8c).

The Archean gneisses and detrital zircons from the biotite schist have variable negative $\varepsilon Hf(t)$ values and old T_{DM}^{C} ages ranging from 3.0 Ga to 4.2 Ga. The significant time gap between the T_{DM}^{C} and crystallization age argues that these silicic rocks were derived from reworking of old mafic continental crust rather than "juvenile" hot subducted slab.

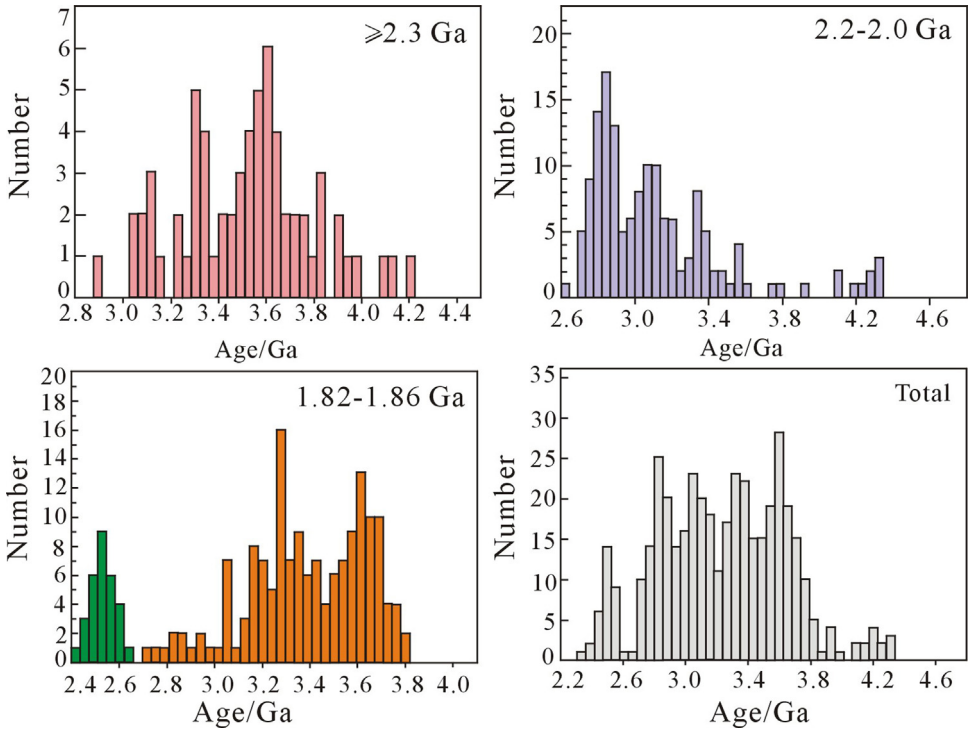

Fig. 10. Histogram of the T_{DM}Hf diagrams (a – the Archean rocks, b – the 2000–2033 Ma gneiss granites and gabbros; c – the massive granites and mafic dyeks; d – the total analyses, see details in the text).

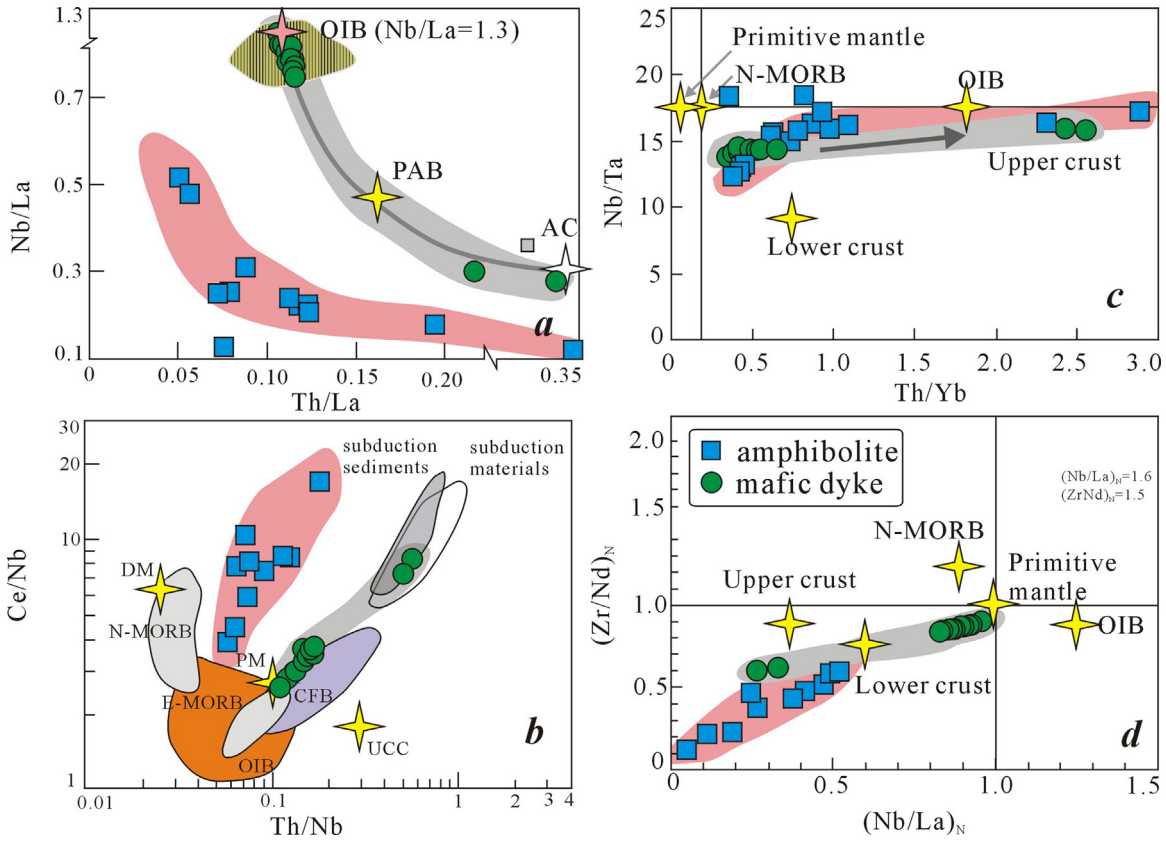

Fig. 12. Binary Harker diagrams for the Archean amphibolites and the late Paleoproterozoic mafic dykes. PAB, primitive arc basalt; AC, average continental crust (PAB and AC was after Kelemen et al., 2004); PM, primitive mantle (Sun and McDonough, 1989); DM, depleted mantle; UC, upper crust; MC, middle crust; LC, lower crust (the UC, MC and LC was after Rudnick and Gao, 2003); CFB, continental flood basalt; OIB, oceanic island basalt; E-MORB, enriched middle ocean ridge basalt; N-MORB, normal middle ocean ridge basalt (Sun and McDonough, 1989) (see details in the text).

Arc magmas can be derived from partial melting of metasomatized mantle wedge underplated at the base of the Archean mafic crust and/or intraplated into the mafic crust, thereby inducing partial melting of the mafic crust at a depth appropriate to stabilize garnet. Subsequent immiscibility between the mafic magma and the sodic adakitic magma (Group I) played an important role during magma ascend (Ray, 2009). Contamination between the magmas affected their geochemical compositions.

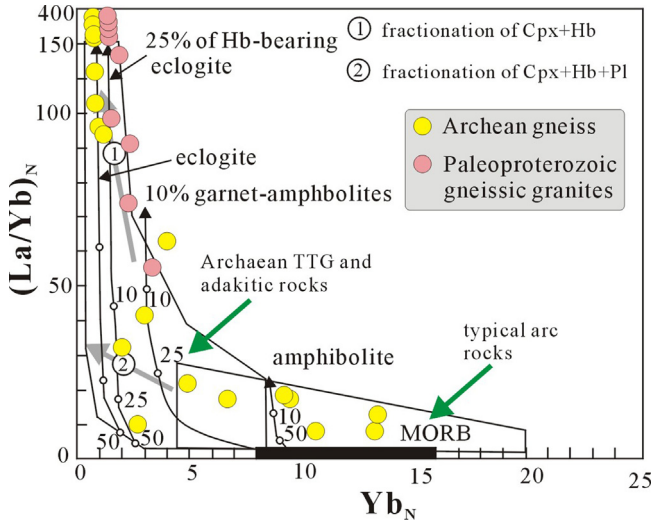

Fig. 13. $(La/Yb)_N$ vs. Yb_N diagram for discriminating adakitic and classic calc-alkaline components.

7.2. The Paleoproterozoic gneissic granites and gneissic gabbros

Trace element compositions of the gneissic granites are marked by high $(La/Yb)_N$ and Sr/Y ratios, showing geochemical similarities to adakitic rocks and resembling with Group I gneisses in this area (Fig. 13). On the other hand, their elevated K_2O contents and high K_2O/Na_2O ratios reveal their difference from those modern adakites and the Archean gneisses (Petford and Gallagher, 2001, Supplementary Table S4). However, elevated K_2O contents could be ascribed to crystal fractionation. Several samples display extremely high Sr/Y ratios (up to 220). The high Sr/Y and (La/Yb)N features of the gneissic granites have been attributed to various contributions of plagioclase, amphibole and/or garnet during melting or fractionation (Huang et al., 2010; Macpherson et al., 2006).

Though it is difficult to distinguish whether garnet and amphibole acted as residual phases during partial melting or as fractionating phases as both processes can induce extraordinary high Sr/Y and La_N/Yb_N ratios, correlation between compatible and incompatible trace elements has been demonstrated to be an effective way of distinguishing fractional crystallization from partial melting (Cocherie, 1986; Li et al., 2013). As scandium decreases rapidly with a relatively small increase in Rb (figure not shown), we suggest that fractional crystallization played a major role in the chemical variations of the gneissic granites. Furthermore, decreases in Al_2O_3, MgO, Fe_2O_3, CaO and TiO_2, with increasing SiO_2 (Fig. 6) also argue for fractional crystallization of garnet, hornblende and

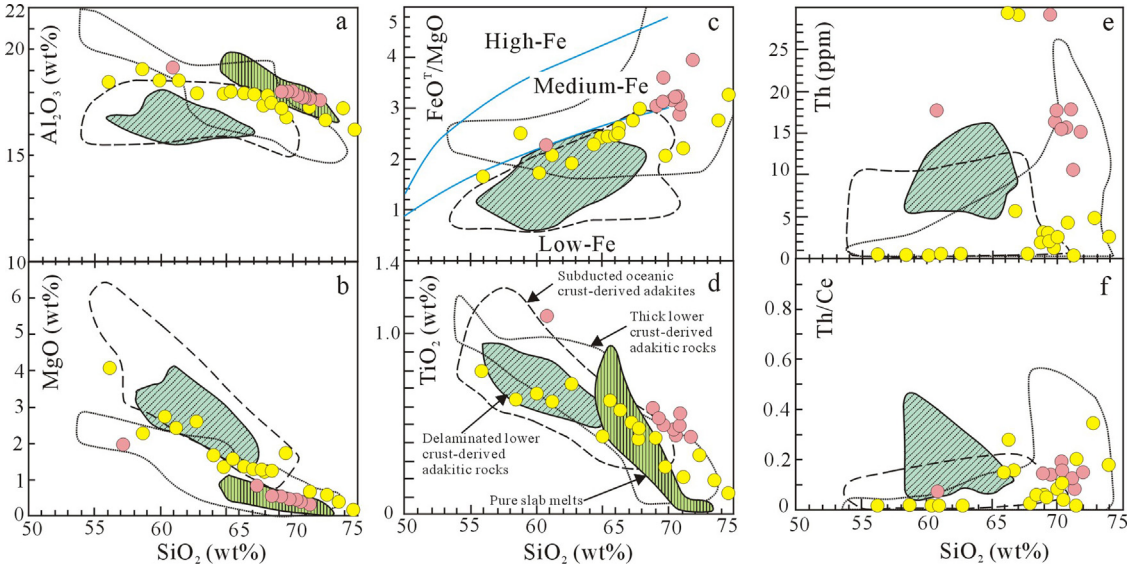

Fig. 14. Harker diagrams showing major and trace element variations of Archean TTG-like gneisses and the Paleoproterozoic gneissic granites. The fields of delaminated lower crust-derived adakitic rocks, subducted oceanic crust-derived adakites, thick lower crust-derived adakitic rocks, and pure slab melts are from Wang et al. (2006).

titanite. Additionally, plagioclase was not the main fractional phase because no significant Eu anomaly was observed on the REE patterns (Fig. 8e).

Based on their geochemical composition, the least evolved sample (AYT05H6) would represent the primitive magma of the gneissic granites. It is dioritic in major element compositions and exhibits typical sodic adakitic composition according to its Sr/Y (73) and $(La/Yb)_N$ (49) ratios. Compared with the adakites derived from partial melting of a subducting oceanic slab or a stalled (or dead) slab in the mantle (Stern and Kilian, 1996; Martin et al., 2005; Defant et al., 2002; Mungall, 2002; Qu et al., 2004; Eyuboglu et al., 2013a,b), this rock has relatively lower MgO, Cr and Ni contents, indicating no significant interaction between the primitive magma with the mantle peridotites (Yogodzinski et al., 1995; Rapp et al., 1999, 2002). Although these features resemble with some of the typical geochemical criteria of adakites generated through slab melting (e.g., low MgO, Cr and Ni contents, Fig. 14 and Supplementary Table S3), their significant difference between crystallization age and the T_{DM}^{C} ages, as well as high Rb/Sr ratios (0.14–0.21, e.g., Huang et al., 2009), rules out this possibility (e.g., Kay and Kay, 1993; Xu et al., 2002; Wang et al., 2004, 2006). Thus, partial melting of mafic rocks in the lower part of thickened crust (Atherton and Petford, 1993; Muir et al., 1995; Petford et al., 1996) was the most viable mechanism for the genesis of these rocks.

Geochemical characteristics of the metagabbros show typical arc-signature geochemistry such as enrichment in LILE and LREE relative to HFSE and HREE, and significant Nb–Ta trough on the spider diagrams (Fig. 8a and b). On the other hand, they exhibit negative to positive $\varepsilon Hf(t)$ values possibly due to crustal contamination. Moreover, we also notice that the gneissic granites have $Mg^{\#}$ ranging from 45 to 57, and some zircons show positive $\varepsilon Hf(t)$, indicative of the possible involvement of mafic magma derived from depleted mantle sources in their genesis. Thus, we suggest that the gneissic granites were mainly derived through high pressure partial melting of a thickened mafic lower crust by underplated/intraplated mafic magma derived from mantle wedge melting.

7.3. The mafic dykes

Two samples (AYT04H5 and AYT04H6) have elevated SiO_2 (54.13–54.55 wt.%), low MgO (3.02–3.13%), $Mg^{\#}$ (29), Cr (9–15 ppm), and Ni (7–8 ppm), indicative of significant fractional crystallization. As shown in Fig. 6, the well-defined negative correlation between CaO, Al_2O_3, MgO with SiO_2 reveals the fractionation of olivine and clinopyroxene. Their elevated LREE, Ba, and Th contents coupled with significant Nb–Ta trough on the primitive mantle normalized spider diagrams (Fig. 7) suggest significant crustal contaminations. These two samples are not used for petrogenetic studies.

The other 13 samples have low SiO_2 (47.8–48.9%), high MgO (6–11.5%), $Mg^{\#}$ (50–70), Cr (92–170 ppm) and Ni (46–106 ppm). These samples are not significantly affected by fractional crystallizations or crustal assimilations. They show similar REE and incompatible elements distribution patterns (Fig. 7). The absence of significant Eu anomalies excludes the fractionation/cumulation of plagioclase during the magma evolution. These samples, in particular the ones with $Mg^{\#}$ greater than 60, can be used to assess the mantle melting conditions.

We have used the dynamic melting inversion (DMI) method (Zou and Zindler, 1996; Zou, 1998; Zou and Reid, 2001) to estimate the degrees of partial melting. The DMI method uses variations of between-magma concentration ratios for two incompatible elements with different partition coefficients, and does not require assumptions about mantle rock concentrations or ratios. Two incompatible trace elements are selected with different partition coefficients, La and Sm. The concentration ratios between a low-degree melt sample (sample AYT03H2) and a high-degree melt sample (sample AYT02H3) are 1.228 (=9.43/7.68) for La and 1.204 (=14.3/11.88) for Sm. Samples AYT03H2 and AYT02H3 are selected because sample AYT03H2 has high incompatible element concentrations (representing the low degree of partial melting) while sample AYT02H3 has low incompatible element concentrations (indicative of high degree of melting). Furthermore, both samples are diabase and have similarl high $Mg^{\#}$ (60–62) to minimize potential effects of fractional crystallization. The degree of partial melting calculated using DMI by solving a system of simultaneous nonlinear equations in Zou et al. (2000) is 6.2% for sample AYT03H2, and 7.4% for sample AYT02H3, using bulk partition coefficients of 0.0029 for La and 0.018 for Sm from Zou and Zindler (1996). If we select these two diabase samples, but use La and Nd pair (instead of La and Sm pair), then the low-degree/high-degree concentration ratios are 1.228 for La and 1.159 (=3.80/3.28) for Nd, and the partial melting degrees using DMI are 5.5% for sample AYT03H2 and 6.6% for sample AYT02H3, using bulk partition coefficients of 0.0029 for

La and 0.0095 for Nd from Zou and Zindler (1996). Averaging the values obtained from La–Sm pair and La–Nd pair yields 5.9% for AYT03H2 and 7.0% for AYT02H3. Thus we infer that these basalts formed by relatively low degrees (6–7%) of mantle partial melting. As stated earlier by Zhang et al. (2002), the DMI method is applicable even when the cogenetic magmas have small compositional variations as a result of small variations in the degrees of partial melting. Note that in the calculations we use concentration ratios instead of elemental abundances, because concentration ratios are insensitive to subsequent fractional crystallizations.

The depth of partial melting is difficult to quantify. The flat HREE patterns in the 13 mafic dykes indicate that garnet is a residual phase in the mantle source. The presence of garnet as a residual mantle phase may suggest that partial melting initiated at >75 km depth in the garnet stability field.

The uncontaminated mafic dykes exhibit trace element signatures similar to those of intraplate basalts, rather than volcanic arc basalts or mid-ocean ridge basalts, based on their enrichment of LREE and insignificant Nb–Ta trough on the incompatible element spider diagram (Fig. 8b). Fig. 12 shows good correlations between some HFSE ratios, i.e., Th/La vs. Nb/La, Ce/Nb vs. Th/Nb, Nb/Ta vs. Th/Yb and $(Nb/La)_N$ vs. $(Zr/Nd)_N$. These mafic dykes have almost identical Nb/La, Th/La, Ce/Nb, Th/Nb and $(Zr/Nb)_N$ ratios to those of the OIB, suggesting that their primitive magmas were derived from an asthenospheric mantle source rather than a metasomatized SCLM source. Both the $\varepsilon Hf(t)$ and $T_{DM}Hf$ (single stage) vary within limited ranges (Figs. 9 and 10 and Supplementary Table S3). In summary, we suggest that the parental magma of the mafic dykes was derived from 6 to 7% partial melting of an OIB-like mantle source at depth >75 km in the garnet stability field. OIB-like basalts may be related to plume magmatism, or to extensional continental intraplate setting [such as the OIB-like East Asian basalts (Basu et al., 1991; Mukasa et al., 1996; Zou et al., 2000)].

7.4. The massive potassic granite

Late Paleoproterozoic potassic granites are widespread and are major constituents of Archean cratons showing great diversity such as CA1-type, CA2-type, sanukitoid suite, A-type and S-type (Sylvester, 1994). Such diversity suggests the involvement of various sources and/or melting at different depths as well as different tectonic scenario (Müller and Groves, 1997; Zhang et al., 2011). Most of the late Paleoproterozoic potassic granites exhibit calc-alkaline or A-type characteristics such as high HREE and HFSE contents, and low Sr/Y and $(La/Yb)_N$ ratios such as in South Africa (e.g., Kampunzu et al., 2003). Sometimes they co-exist with the sanukitoid suite which is most likely derived from previously metasomatised mantle (Kampunzu et al., 2003; Martin et al., 2005).

The potassic granites in this study have high SiO_2 and total alkali, and exhibit very large range of total REE and other incompatible elements (Fig. 8i and j and Supplementary Table S3). Sample AYT006H3 has the highest total REE (3082 ppm) and Zr, Sr, Y contents while sample AYT006H4 has the lowest total REE contents (37.7 ppm), similar to those of S-type granites. Thus, this scenario is very similar to the early Paleoproterozoic gneissic granitic intrusive complex in southern Tarim (Zhang et al., 2007b).

Based on their high SiO_2, Al_2O_3, $Na_2O + K_2O$ and low MgO, TiO_2, Fe_2O_3 and HFSE, especially their Archean zircon Hf model ages and the pronounced enriched $\varepsilon Hf(t)$ values (−11 to ~−15), we infer that the massive potassic granites were derived from partial melting of the Archean andesitic-silicic crust at relatively shallow depth. Moreover, their outcrop features (occurring as small plutons and dykes with massive structure) as well as their close spatial and temporal relationship with the mafic dyke swarms could well account for the heat for the partial melting of the Achaean gneisses.

8. Tectonic implications

8.1. The Archean tectonic evolution

Geochronological and geochemical data on the Neoarchean amphibolite-TTG gneiss in Aketage area show the following salient features: (1) coeval arc-signature for the tholeiitic amphibolite, and tonalite–trondhjemite–granodiorite–granite originating from different magma sources; and (2) ~2.5 Ga metamorphic event as revealed by zircon U–Pb dating.

The tectonic setting of Archean TTG rocks is a topic of continued debate (Smithies, 2000; Kamber and Collerson, 2000; Condie, 2005; Martin, 1999; Martin et al., 2005; Bindeman et al., 2005; Naqvi and Prathap, 2007; Santosh et al., 2013a). The synchronous formation of TTG and greenstone belts was considered to be a consequence of oceanic arc – oceanic arc collision (Kunugiza et al., 1996; Martin et al., 2005; Naqvi and Prathap, 2007; Zhai and Santosh, 2011; Manikyamba and Kerrich, 2012). We suggest that the intermingled amphibolites and TTG gneisses in Aketage area were most possibly formed in an arc setting based on the following evidence. (1) The amphibolites occurring within the gneisses possess geochemical signature of arc tholeiite and were most likely derived from a metasomatized lithospheric mantle (mantle wedge) above a subduction zone; (2) since Achaean was an era of higher geothermal regime, partial melting of the mafic lower crust under an arc system is possible, especially with thermal input from a mafic magma derived from the mantle wedge. The TTGs are closely associated in time and space with the amphibolites, and there is no evidence for any difference in tectonic settings between these rocks; (3) the TTGs also exhibit characteristics of volcanic arc granites, such as their low Rb, Nb and Y and high Al_2O_3 contents; (4) the ~2.5 Ga metamorphic event revealed by the overgrowth mantle of the magmatic zircons from the TTGs and the biotite-quartz schist (supracrustal rock), which is documented in this study for the first time in Tarim block, argue for a possible collisional event at the end of the Archean. Therefore, a Neoarchean subduction-collision event is suggested.

8.2. Late Paleoproterozoic orogenic event: new insight

In the Aketage area, the gneissic granites exhibit systematic I-type granite signature as well as adakite-like features, indicating they were formed at an arc setting. Two samples of the 2033 Ma gabbro also exhibit typical arc signatures. Moreover, the Archean rocks in the area show a ~2.0 Ga metamorphic event (Liu et al., 2010 and this study). Thus it is reasonable to deduce that the Paleoproterozoic subduction lasted till ~2.0 Ga followed by collision. The OIB-like mafic dyke swarm and the massive potassic granites, as well as the coeval mafic dyke swarm in southern margin of the Qaidam block (Lu et al., 2008), suggest an extensional tectonic system at ca. 1.86 Ga, suggesting post-orogenic extension in Aketage area following the collisional event.

In Quruqtagh area, recent studies have revealed that both the 2.60–2.53 Ga Achaean (Tuoge complex) and the amphibolite to granulite facies Paleoproterozoic gneiss-schist belt (Quruqtage complex) were metamorphosed at ca. 1.85–1.80 Ga (Zhang et al., 2012b; Ge et al., 2013). In the Dunhuang area, He et al. (2013) reported ~2.0 Ga mafic rocks with arc-signature and ~1.85 Ga granulite-facies metamorphic event, which are well consistent with the ~1.94 Ga arc-signature of the granodiorite-granite suite and the ~1.85 Ga amphibolite facies metamorphic event in Quruqtagh, probably related to the collision event associated with the assembly of the Columbia supercontinent (Lei et al., 2012; Zhang

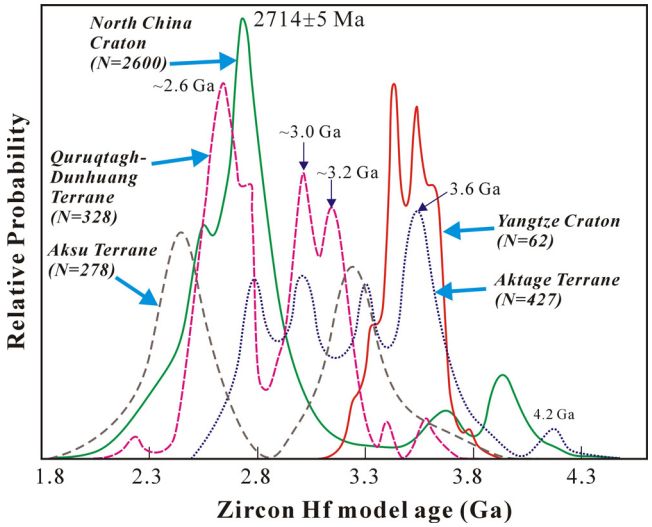

Fig. 15. Zircon Hf model age spectra of the Quruqtagh-Dunhuang terrane and Aketage-Qaidam terrane of the Tarim, North China and Yangtze Cratons (the data of the Quruqtagh-Dunhuang terrane are from Long et al., 2010; He et al., 2013; Zhang et al., 2013a; data of the North China Craton are from Geng et al., 2012 and references therein; data of the Continental nuclei of the Yangtze Block were from Zhang et al., 2006b; Jiao et al., 2009, see detailed discussion in the text).

et al., 2013a). Moreover, ~1.75 Ga magmatism in the Dunhuang area shows a mixture of reworked Archean crust with juvenile magmas, and is probably related to a post-collisional episode (He et al., 2013).

In southwestern Tarim Craton, the oldest basement rocks dated so far is the 2.41–2.34 Ga Heluositan intrusive complex (Zhang et al., 2007b). The overgrowth mantles of the 2.41 Ga magmatic zircons yield well-defined concordant age of 1.9 Ga. This age represents the late Paleoproterozoic orogenic event in southwestern Tarim Craton.

In summary, our study shows that the late Paleoproterozoic orogenic events in different terranes of the Tarim Craton were not coeval. The orogenic events associated with collision in Aketage-Qaidam terrane, the southwestern Tarim terrane and Quruqtagh-Dunhuang terrane, took place at ca. 2.0 Ga, ca. 1.9 Ga and ca. 1.85–1.80 Ga, respectively. These ages are broadly similar to the diachronous collisional events reported from the North China Craton during the final assembly of the continental blocks in late Paleoproterozoic (Santosh et al., 2012, 2013b; Zheng et al., 2013; Zhao and Zhai, 2013).

8.3. Continental crust growth process

Zircon Hf isotope compositions of the diverse rocks from Aketage area show that growth of the early Precambrian continental crust mainly took place during 2.7–4.3 Ga with peaks at 2.8 Ga, 3.1 Ga, 3.3 Ga, 3.6 Ga and 4.2 Ga (Fig. 15). In combination with their $\varepsilon Hf(t)$ values, the most silicic rocks represent recycled products of the Archean rocks. Importantly, ~3.6 Ga xenocrystic zircons were documented in a ~2.0 Ga gneissic granite pluton (Lu et al., 2008). Thus, we deduce the existence of Paleoarchean and even Hadean crust in the Aketage area.

In Quruqtagh-Dunhuang terrane, zircon Hf isotope studies revealed that the early Precambrian continental crust growth took place mainly during 2.6–3.6 Ga with major peaks at ca. 2.6–2.8 Ga, 3.0 Ga, 3.2 Ga and minor peaks at ca. 3.4 Ga and 3.6 Ga (Fig. 15). In northwestern Tarim Craton, the exposed oldest rock is the blueschist in the Aksu Group, and our unpublished data show that crustal residence ages of the ca. 1.9 Ga detrital zircons mainly range from 2.9 Ga to 4.0 Ga with a single peak at 3.3 Ga (Fig. 15). For southwestern Tarim Craton, no zircon Hf isotope data exist.

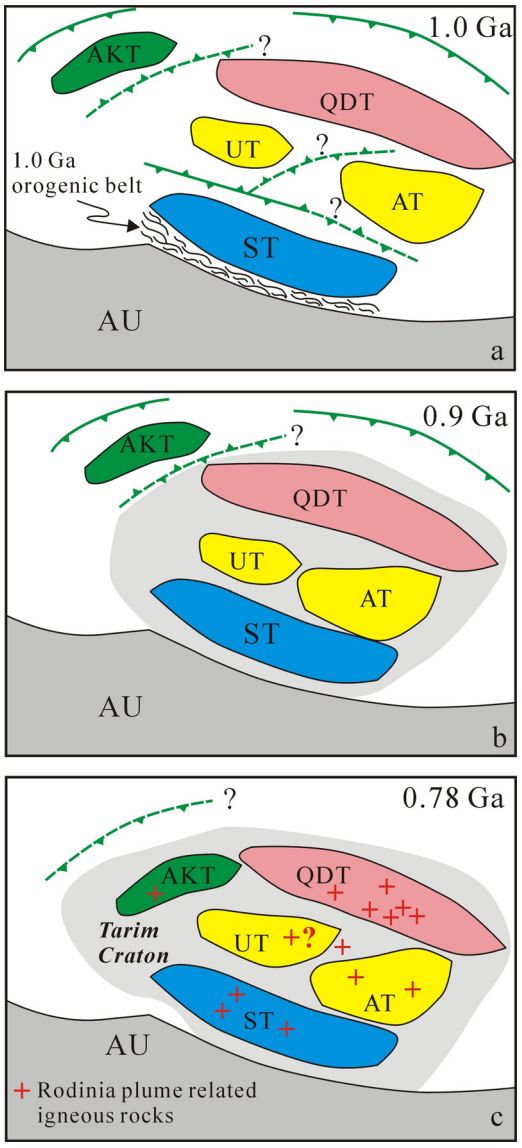

Fig. 16. Discrete terranes of the Precambrian basement of the Tarim Craton amalgamated together in the early to middle Neoproterozoic forming the unified Precambrian basement of the Tarim Craton. AU, Australia Craton; AKT, Aksu terrane; QDT, Quruqtagh, Dunhuang terrane; AT, Aketage-(Qaidam) terrane; ST, South Tarim terrane; UT, possible unknown terrane/terranes in central Tarim. The solid and dashed lines with one side sawtooth represent reliable/possible subduction zone with known orientation, while the solid/dashed line with double side sawtooth represents reliable/possible subduction zone with unknown orientation.

8.4. Multiple discrete terranes of the Precambrian basement of Tarim

Recently, Xu et al. (2013) divided the >900 Ma rocks in the Tarim Precambrian basement into three main tectonic units: the North Tarim terrane, the southern Tarim terrane and the Neoproterozoic central suture zone. However, the distinct crustal growth history during early Precambrian in the different terranes of Tarim might suggest that these terranes were derived from various cratonic nuclei, which were finally unified into the Precambrian basement of this craton by early Neoproterozoic during the assembly of the Rodinia supercontinent (Fig. 16). This inference is based on the evidence that: (1) all these terranes share a common Neoproterozoic cover sequence but have very different Pre-Nanhuaian basements; (2) they show significant time difference in the Paleoproterozoic orogenic events; and (3) they have different early Precambrian continental growth processes.

Based on a comprehensive synthesis on the global Paleoproterozoic orogenic events, Zhao et al. (2002) and Rogers and Santosh (2002) reconstructed the configuration of the Columbia supercontinent (see Meert, 2014; Nance et al., 2014 for recent reviews). In this model, the cratonic blocks in South America and West Africa were welded by the 2.1-2.0 Transamazonia and Eburnean Orogens, the Kaapvaal and Zimbabwe Cratons in southern Africa were collided along the ~2.0 Ga Limpopo Belt (Rogers and Santosh, 2002, 2009). In the Yangtze Block of South China, recent studies indicate that the Archean Kongling complex was overprinted by 2.03–1.97 Ga granulite facies metamorphism and it was subsequently intruded by ~1.85 Ga mafic dykes and A-type granites with intraplate-signature (Ling et al., 2001; Zhang et al., 2006a,b; Xiong et al., 2009; Peng et al., 2009). Based on detrital zircon U–Pb dating of the Mesoproterozoic rocks in western Yangtze, Chen et al. (2013a,b) suggested that the Yangtze Block was likely linked with the North Australia Craton in Columbia during late Paleoproterozoic. On the other hand, the other Paleoproterozoic orogenic events documented in Australia, North America, Atlantic and Baltica mostly took place during 1.9–1.8 Ga. The central India tectonic zone was most possibly connected with the trans-North China Orogen and the collision took place at ~1.85 Ga (Zhao et al., 2002), though the detailed orogenic process remains equivocal (Santosh et al., 2006, 2007; Santosh, 2010; Zhao et al., 2012).

The initial extension event after the assembly of the Columbia supercontinent began at ~1.85 Ga (Hou et al., 2008). The earliest extension-related igneous activities have been documented from the North China Craton, Canadian Shield, South Indian Craton and the Yangtze Block (Zhao et al., 2002 and references therein; Peng et al., 2009). In the North China Craton, the early unmetamorphosed and undeformed mafic dykes occur in the Xionger group along the southern part of the craton, with the oldest zircon U–Pb age of 1841 ± 18 Ma (Hou et al., 2006). In the Canadian Shield, the age of the Sparrow mafic dykes is 1839 ± 5 Ma (Halls and Heaman, 2000) and in the Southern India Craton, the Late Paleoproterozoic dykes extend from south to north in various crustal blocks. Among these dykes, the Dharmapuri mafic dykes yielded a $^{40}Ar/^{39}Ar$ age of 1855 ± 9 Ma, representing unmetmorphosed and undeformed mafic dykes swarm (Radhakrishna et al., 1999, 2007). Based on these data, Hou et al. (2008) suggested that the ~1.85 Ga mafic dyke swarm in the North China Craton, Canadian Shield and the Southern Indian Craton, composed a radiating dyke swarm were centered at Xionger, and that the radiating dyke swarm was genetically related to a mantle plume (Santosh et al., 2009).

The ~1.85 Ga mafic dyke swarm in Aketage and in the southern margin of the Qaidam block could be part of this global radiating dyke swarm (Zhang et al., 2013a,b). The tectonic settings and affinity of the Aketage-Qaidam terrane must satisfy two prerequisites: that the orogenic event took place at ~2.0 Ga and the first pulse of extension-related igneous activity took place at ~1.85 Ga, after the ~2.0 Ga collisional event. The North China and South India Craton were excluded because the coeval orogenic events of ca. 1.85 Ga occur in the Central Indian Tectonic Zone and in the Trans North China Orogen (Zhao et al., 2002, 2010). The ~2.0 Ga metamorphism and ~1.85 Ga mafic dykes and A-type granites in the Yangtze continental nuclei (the Kongling complex) are consistent with the scenario of the correlation between the Aketage-Qaidam terrane and they were likely connected in the Columbia supercontinent. Moreover, according to the detrital zircon U–Pb age spectra comparison, Chen et al. (2013a) speculated that the Yangtze Block could be connected with the North Australia Craton.

On the other hand, the Quruqtagh-Dunhuang terrane, as well as the Quanji massif, show significant affinity with that of the North China and the Southern India Cratons, including the intrusion of the late Archean potassic granites (Shang et al., 2010; Zhou et al., 2011), and ~1.85 Ga collisional event (Chen et al., 2013b). Thus, we conclude that the Aketage-Qaidam terrane was most possibly a continental fragment detached from the Yangtze-North Australia Craton (Fig. 16), whereas the Quruqtagh-Dunhuang terrane could be a continental fragment detached from the North China-India amalgam (Fig. 16).

Due to limited information on the geology and geochronology of the southwestern terrane, the affinity of this terrane is not well constrained though we could confirm ~1.9 Ga collision orogenic event in this terrane. This terrane shows significant difference with the Quruqtagh-Dunhuang terrane and the Aketage-Qaidam terrane. Thus, we suggest the possibility that this is an independent terrane rather than a fragment of northern Tarim (e.g., Xu et al., 2013).

Both field mapping and detrital zircon U–Pb dating indicate the absence of Archean basement of the Aksu terrane (Xinjiang, 1993; Zhang et al., 2014). Thus, the Aksu terrane could be an early to middle Neoproterozoic accretionary terrane amalgamated to the fringe of the Tarim Craton during 820–780 Ma according to the ages of the blue-schist facies metamorphism and geochemistry of the mafic volcanic rocks in the Aksu terrane (Yong et al., 2013; Liou et al., 1996) (Fig. 16c). In addition, since the large area of the central Tarim Craton is covered by desert, unknown terrane/terranes in central Tarim Craton is/are possible (Fig. 16).

9. Conclusions

(1) The Milan Group in Aketage mainly comprises 2.7–2.5 Ga gneissic amphibolite–TTG complex and minor paragneiss. The ca. 2.5 Ga metamorphism represents the formation of the protocrust of the Aketage terrane.
(2) The 2.01–2.03 Ga arc-affinity of the gneissic granites and gabbros, as well as the commonly observed 2.0 Ga metamorphic event revealed by zircon U–Pb dating, suggest a subduction-collision tectonic evolution process. The ca. 1840–1867 Ma massive potassic granites, OIB-like mafic dyke swarm and massive leucogranite dykes argue for an extensional tectonic system. The OIB-like mafic dyke swarm is coeval with the dyke swarms in the North China Craton, Canadian Shield and Southern Indian Craton, and could be genetically related to the first pulse of mantle plume after the amalgamation of the Columbia supercontinent.
(3) Significant temporal discrepancy of late Paleoproterozoic orogenic events for the different terranes in Tarim Craton was revealed. Collision orogenic event took place at 1.85–1.80 Ga in Quruqtagh-Dunhuang terrane, at 1.90 Ga in the Southwestern Tarim terrane, and at ca. 2.0 Ga in the Aketage-Qaidam terrane. Moreover, the Quruqtagh-Dunhuang terrane and the Aketage-Qaidam terrane show distinct timings in continental growth process. The Aketage-Qaidam terrane was possible a continental fragment detached from the Yangtze – North Australia Craton whereas the Quruqtagh-Dunhuang terrane was possibly linked to the North China – India Craton during the assemblage of the Columbia supercontinent.
(4) The discrete Precambrian terranes of the Tarim, including the Quruqtagh-Dunhuang terrane, the Aketage-Qaidam terrane, Southwestern Tarim terrane and the Aksu terrane, were amalgamated possibly during early Neoproterozoic to form the unified Precambrian basement of the Tarim Craton. Before this amalgamation, a unified Tarim Craton did not exist.

Acknowledgements

We thank Prof. Song-Nian Lu for his kind help with the interpretation of the geochronological data and Mr. Ni-Kang for his help with the field works. We are grateful to Prof. C. Manikyamba, Prof.

Wenjiao Xiao, Prof. Guochun Zhao and two anonymous reviewers for their critical comments and constructive suggestions that have significantly improved the quality of this paper. This work was supported by National Science Foundation of China (41172175) and Foundation of State Key Laboratory of Continental Tectonics and Dynamics of China, CAGS (201306). This study also contributes to the Talent Award to M. Santosh under the 1000 Talents Plan of the Chinese Government.

References

Atherton, M.P., Petford, N., 1993. Generation of sodium-rich magmas from newly underplated basaltic crust. Nature 362, 144–146.

Bagas, L., Næraa, T., Kolb, J., Reno, B., Fiorentini, M.L., 2013. Partial melting of the Archaean Thrym Complex of southeastern Greenland. Lithos 160–161, 164–182.

Basu, A.R., Wang, J.W., Huang, W.K., Xie, G.H., Tatsumoto, M., 1991. Major element, REE, and Pb, Nd and Sr isotopic geochemistry of Cenozoic volcanic rocks of eastern China: implications for their origin from suboceanic-type mantle reservoirs. Earth Planet. Sci. Lett. 105, 149–169.

Bindeman, I.N., Eiler, J.M., Yogodzinski, G.M., Tatsumi, Y., Stern, C.R., Grove, T.L., Portnyagin, M., Hoernle, K., Danyushevsky, L.V., 2005. Oxygen isotope evidence for slab melting in modern and ancient subduction zones. Earth Planet. Sci. Lett. 235, 480–496.

Chen, W.T., Zhou, M.F., Zhao, X.F., 2013a. Late Paleoproterozoic sedimentary and mafic rocks in the Hekou area SW China: implication for the reconstruction of the Yangtze Block in Columbia. Precambrian Res. 231, 61–77.

Chen, N.S., Liao, F., Wang, L., Santosh, M., Sun, M., Wang, Q., Mustafa, H.A., 2013b. Late Paleoproterozoic multiple metamorphic events in the Quanji Massif: links with Tarim and North China Cratons and implications for assembly of the Columbia supercontinent. Precambrian Res. 228, 102–116.

Cocherie, A., 1986. Systematic use of trace-element distribution patterns in log–log diagrams for plutonic suites. Geochim. Cosmochim. Acta 50, 2517–2522.

Condie, K.C., 2005. TTGs and adakites: are they both slab melts? Lithos 80, 33–44.

Defant, M.J., Xu, J.F., Kepezhinskas, P., Wang, Q., Zhang, Q., Xiao, L., 2002. Adakites: some variations on the theme. Acta Petrol. Sin. 18, 129–142.

Eyuboglu, E., Dudas, F.O., Santosh, M., Yi, K., Kwon, S., Akryali, E., 2013a. Petrogenesis and U–Pb zircon chronology of adakitic porphyries within the Kop ultramafic massif (Eastern Pontides Orogenic Belt, NE Turkey). Gondwana Res. 24, 742–766.

Eyuboglu, Y., Santosh, M., Dudas, F.O., Akryali, E., Chung, S.L., Akdag, K., Bektas, O., 2013b. The nature of transition from adakitic to non-adakitic magmatism in a slab window setting: a synthesis from the eastern Pontides, NE Turkey. Geosci. Front. 4, 353–375.

Finch, R.J., Hanchar, J.M., 2003. Structure and chemistry of zircon and zircon-group minerals. Rev. Mineral. Geochem. 53, 1–25.

Geng, J.Z., Li, H.K., Zhang, J., Zhang, Y.Q., 2011. Zircon Hf isotope analysis by means of LA-MC-ICP-MS. Geol. Bull. China 30, 1508–1513 (in Chinese with English abstract).

Geng, Y.S., Du, L.L., Ren, L.D., 2012. Growth and reworking of the early Precambrian continental crust in the North China Craton: constraints from zircon Hf isotopes. Gondwana Res. 21, 517–529.

Ge, R.F., Zhu, W.B., Wu, H.L., Zheng, B.H., He, J.W., 2013. Timing and mechanisms of multiple episodes of migmatization in the Korla Complex, northern Tarim Craton, NW China: constraints from zircon U–Pb–Lu–Hf isotopes and implications for crustal growth. Precambrian Res. 231, 136–156.

Halls, H.C., Heaman, L.M., 2000. The paleomagnetic significance of new U–Pb age data from the Molsen dyke swarm, Cauchon Lake area, Manitoba. Can. J. Earth Sci. 37, 957–966.

He, Z.Y., Zhang, Z.M., Zong, K.Q., Dong, X., 2013. Paleoproterozoic crustal evolution of the Tarim Craton: constrained by zircon U–Pb and Hf isotopes of meta-igneous rocks from Korla and Dunhuang. J. Asian Earth Sci. 78, 54–70.

Hoskin, P.W., Schaltegger, U., 2001. The composition of zircon and igneous and metamorphic petrogenesis. Rev. Mineral. Geochem. 53, 25–104.

Hou, G.T., Liu, Y., Li, J., Qian, X., 2006. Evidence for ~1.8 Ga extension of the Eastern Block of the North China Craton from SHRIMP U–Pb dating of mafic dyke swarms in Shandong Province. J. Asian Earth Sci. 27, 392–401.

Hou, G.T., Santosh, M., Qian, X.L., Lister, G.S., Li, J.H., 2008. Configuration of the Late Paleoproterozoic supercontinent Columbia: insights from radiating mafic dyke swarms. Gondwana Res. 14, 395–409.

Hou, K.J., Li, Y.H., Tian, Y.R., 2009. In situ U–Pb zircon dating using laser ablation-multi ion counting ICP-MS. Mineral Depos. 28, 481–492 (in Chinese with English abstract).

Huang, X.L., Xu, Y.G., Lan, J.B., Yang, Q.J., Luo, Z.Y., 2009. Neoproterozoic adakitic rocks from Mopanshan in the western Yangtze Craton: partial melts of a thickened lower crust. Lithos 112, 367–381.

Huang, X.L., Niu, Y.L., Xu, Y.G., Yang, Q.J., Zhong, J.W., 2010. Geochemistry of TTG and TTG like gneisses from Lushan–Taihua complex in the southern North China Craton: implications for late Archean crustal accretion. Precambrian Res. 182, 43–56.

Huang, X.L., Wilde, S.A., Yang, Q.J., Zhong, J.W., 2012. Geochronology and petrogenesis of gray gneisses from the Taihua Complex at Xiong'er in the southern segment of the Trans-North China Orog: implications for tectonic transformation in the Early Paleoproterozoic. Lithos 134-135, 236–252.

Jiao, W.F., Wu, Y.B., Yang, S.H., Peng, M., Wang, J., 2009. The oldest basement rock in the Yangtze Craton revealed by zircon U–Pb age and Hf isotope composition. Sci. China D: Ser. 52, 1393–1399.

Kamber, B.S., Collerson, K.D., 2000. Role of "hidden" deeply subducted slabs in the mantle depletion. Chem. Geol. 166, 241–254.

Kampunzu, A.B., Tombale, A.R., Zhai, M., Bagai, Z., Majaule, T., Modisi, M.P., 2003. Major and trace element geochemistry of plutonic rocks from Francistown NE Botswana: evidence for a Neoarchaean continental active margin in the Zimbabwe craton. Lithos 71, 431–460.

Kay, R.W., Kay, S.M., 1993. Delamination and delamination magmatism. Tectonophysics 219, 177–189.

Kerrich, R., Polat, A., 2006. Archaean greenstone–tonalite duality: thermochemical mantle convection models or plate tectonics in the early Earth global dynamics? Tectonophysics 415, 141–165.

Kelemen, P.B., Hanghoj, K., Greene, A.R., 2004. One view of the geochemistry of subduction-related magmatic arcs, with an emphasis on primitive andesite and lower crust. In: Rudnick, R.L. (Ed.), Treatise on Geochemistry, vol. 3. Elsevier Pergamon, Amsterdam, pp. 593–659.

Kemp, A.I.S., Hawkesworth, C.J., 2003. Granitic perspectives on the generation and secular evolution of the continental crust. In: Rudinick, R.L. (Ed.), Treaties on Geochemistry, vol. 3, pp. 349–410.

Kunugiza, K., Kate, Y., Kane, T., Takaba, Y., Kuruma, I., Sohma, T., 1996. An Archaean tectonic model of the Dharwar craton, southern India: the origin of the Holenarasipur greenstone belt (Hussan district Karnataka) and reinterpretation of the Sargur–Dharwar relationship. J. Southeast Asian Earth Sci. 14, 149–160.

Lee, Y., Cho, M., 2013. Fluid-present disequilibrium melting in Neoarchean arc-related migmatites of Daeijak Island, western Gyeonggi Massif, Korea. Lithos 179, 249–262.

Lei, R.X., Wu, C.Z., Chi, G.X., Chen, G., Gu, L.X., Jiang, Y.H., 2012. Petrogenesis of the Palaeoproterozoic Xishankou pluton, northern Tarim block, northwest China: implications for assembly of the supercontinent Columbia. Int. Geol. Rev. 54, 1829–1842.

Li, X.H., Li, Z.X., Li, W.X., Wang, X.C., Gao, Y.Y., 2013. Revisiting the "C-type adakites" of the Lower Yangtze River Belt, central eastern China: in-situ zircon Hf–O isotope and geochemical constraints. Chem. Geol. 345, 1–15.

Li, X.H., Liu, D.Y., Sun, M., Li, W.X., Liang, X.R., Liu, Y., 2004. Precise Sm-Nd and U–Pb isotopic dating of the super-giant Shizhuyuan polymetallic deposit and its host granite, Southeast China. Geol. Mag. 141, 225–231.

Ling, W.L., Gao, S., Zhang, B.R., Zhou, L., Xu, Q.D., 2001. The recognizing of ca. 1.95 Ga tectono-thermal eventin Kongling nucleus and its significance for the evolution of Yangtze Block South China. Chin. Sci. Bull. 46 (4), 326–329.

Liu, Y.S., Xin, H.T., Zhou, S.J., Teng, X.J., Yang, J.Q., Lu, H.Q., 2010. Precambrian and Phanerozoic Tectonic Evolution of the Lapeiquan Area in Eastern Altyn Mountain. Geological Publishing House, Beijing, pp. 7–47.

Liou, J.G., Graham, S.A., Maruyama, S., Zhang, R.Y., 1996. Characteristics and tectonic significance of the late Proterozoic Aksu blueschists and diabasic dikes northwest Xinjiang, China. Int. Geol. Rev. 38, 228–244.

Long, X.P., Yuan, C., Sun, M., Zhao, G.C., Xiao, W.J., Wang, Y.J., Yang, Y.H., Hu, A.Q., 2010. Archean crustal evolution of the northern Tarim craton NW China: zircon U–Pb and Hf isotopic constraints. Precambrian Res. 180, 272–284.

Long, X.P., Yuan, C., Sun, M., Xiao, W.J., Zhao, G.C., Zhou, K.F., Wang, Y.J., Hu, A.Q., 2011a. The discovery of the oldest rocks in the Kuluketage area and its geological implications. Sci. China D: Ser. 54, 342–348.

Long, X.P., Yuan, C., Sun, M., Kröner, A., Zhao, G.C., Wilde, S., Hu, A.Q., 2011b. Reworking of the Tarim Craton by underplating of mantle plume-derived magmas: evidence from Neoproterozoic granitoids in the Kuluketage area NW China. Precambrian Res. 187, 1–14.

Lu, S.N., 1992. Proterozoic Tectonic Evolution of the Quruqtagh, vols. 26–27. Publication of Tianjin Institute of Geology and Mineral Resources, Xinjiang, pp. 279–292 (in Chinese).

Lu, S.N., Yu, H.F., Zhao, F.Q., 2002. Preliminary Study of Precambrian Geology in the North Tibet—Qinghai Plateau. Geological Publishing House, Beijing, pp. 2–87 (in Chinese).

Lu, S.N., Yuan, G.B., 2003. Geochronology of early Precambrian magmatic activities in Aketasdhtage, east Altyn tagh. Acta Geol. Sin. 77, 61–68 (in Chinese with English abstract).

Lu, S.N., Li, H.K., Zhang, C.L., Liu, G.H., 2008. Geological and geochronological evidences for the Precambrian evolution of the Tarim Craton and surrounding continental fragments. Precambrian Res. 160, 94–107.

Ludwig, K.R., 1999. Using Isoplot/EX, Version 2, A Geolocronolgical Toolkit for Microsoft Excel. Berkeley Geochronological Center Special Publication 1a, pp. 47.

Ludwig, K.R., 2001. Squid 1.02: A User Manual. Berkeley Geochronological Center Special Publication l2, pp. 19.

Macpherson, C.G., Dreher, S., Thirlwall, M.F., 2006. Adakites without slab melting: high pressure differentiation of island arc magma, Mindanao, the Philippines. Earth Planet. Sci. Lett. 243, 581–593.

Manikyamba, C., Kerrich, R., 2012. Eastern Dharwar Craton India: continental lithosphere growth by accretion of diverse plume and arc terranes. Geosci. Front. 3, 225–240.

Martin, H., 1999. Adakitic magmas: modern analogues of Archaean granitoids. Lithos 46, 411–429.

Martin, H., Moyen, J.-F., 2003. Secular changes in TTG composition: comparison with modern adakits. EGS-AGU-EUG Joint Meeting, Nice, April, VGP7-1FR2O-001.

Martin, H., Smithies, R.H., Rapp, R., Moyen, J.-F., Champion, D., 2005. An overview of adakite, tonalite–trondhjemite–granodiorite (TTG), and sanukitoid: relationships and some implications for crustal evolution. Lithos 79, 1–24.
Meert, J.G., 2014. Strange attractors, spiritual interlopers and lonely wanderers: the search for pre-Pangean supercontinents. Geosci. Front. 5, 155–166.
Muir, R.J., Weaver, S.D., Bradshaw, J.D., Eby, G.N., Evans, J.A., 1995. The Cretaceous Separation Point batholith, New Zealand: granitoid magmas formed by melting of mafic lithosphere. J. Geol. Soc. Lond. 152, 689–702.
Mukasa, S.B., Fischer, G.M., Barr, S.M., 1996. In: Basu, A.R., Hart, S.R. (Eds.), The Character of the Subcontinental Mantle in Southeast Asia: Evidence from Isotopic and Elemental Compositions of Extension-related Cenozoic Basalts in Thailand. American Geophysical Union, Washington, pp. 233–252.
Mungall, J.E., 2002. Roasting the mantle: slab melting and the genesis of major Au and Au-rich Cu deposits. Geology 30, 915–918.
Müller, D., Groves, D.I. (Eds.), 1997. Potassic Igneous Rocks and Associated Gold–Copper Mineralization. Springer-Verlag, Berlin Heidelberg, pp. 1–225.
Nance, R.D., Murphy, J.B., Santosh, M., 2014. The supercontinent cycle: a retrospective essay. Gondwana Res. 25, 4–29.
Naqvi, S.M., Prathap, J.G.R., 2007. Geochemistry of adakites from Neoarchaean active continental margin of Shimoga schist belt, Western Dharwar craton, India: implications for genesis of TTG. Precambrian Res. 156, 32–54.
Pearce, J.A., Cann, J.R., 1973. Tectonic setting of basic volcanic rocks determined using trace element analyses. Earth Planet. Sci. Lett. 19, 290–300.
Pearce, J.A., Thirlwall, M.F., Ingram, G., Murton, B.J., Arculus, R.J., Van der Laan, S.R., 1992. Isotopic evidence for the origin of Boninites and related rocks drilled in the Izu-Bonin (Ogasawara) forearc Leg 125. In: Fryer, P., Pearce, J.A., Stokking, L. (Eds.), Proceedings of the Ocean Drilling Program Scientific Results, vol. 125, pp. 237–261.
Pearce, J.A., 2008. Geochemical fingerprinting of oceanic basalts with applications to ophiolite classification and the search for Archean oceanic crust. Lithos 100, 14–48.
Peng, M., Wu, Y.B., Wang, J., Jiao, W.F., Liu, X.C., Yang, S.H., 2009. Paleoproterozoic mafic dyke from Kongling terrain in the Yangtze Craton and its implication. Chin. Sci. Bull. 54, 1098–1104.
Petford, N., Atherton, M.P., Halliday, A.N., 1996. Rapid magma production rates, underplating and remelting in the Andes: isotopic evidence from northern-central Peru (90–110s). J. South. Am. Earth Sci. 9, 69–78.
Petford, N., Gallagher, G., 2001. Partial melting of mafic (amphibolitic) lower crust by periodic influx of basaltic magma. Earth Planet. Sci. Lett. 193, 483–499.
Peacock, S.M., Rushmer, T., Thompson, A.B., 1994. Partial melting of subducting oceanic crust. Earth Planet. Sci. Lett. 121, 224–227.
Qu, X.M., Hou, Z.Q., Li, Y.G., 2004. Melt components derived from a subducted slab in late orogenic ore-bearing porphyries in the Gangdese copper belt, southern Tibetau plateau. Lithos 74, 131–148.
Radhakrishna, T., Maluski, H., Mitchell, J.G., Joseph, M., 1999. $^{40}Ar/^{39}Ar$ and K/Ar geochronology of the dykes from the south Indian granulite terrain. Tectonophysics 304, 109–129.
Radhakrishna, Krishnendu, N.R., Balasubramonian, G., 2007. Mafic dyke magmatism around the Cuddapah Basin: age constraints, petrological characteristics and geochemical inference for a possible magma chamber on the southwestern margin of the basin. J. Geol. Soc. India 70, 194–206.
Rapp, R.P., Shimizu, N., Norman, M.D., Applegate, G.S., 1999. Reaction between slab-derived melts and peridotites in the mantle wedge: experimental constraints at 3.8 GPa. Chem. Geol. 160, 335–356.
Rapp, R.P., Xiao, L., Shimizu, N.M., 2002. Experimental constraints on the origin of potassium-rich adakities in east China. Acta Petrol. Sin. 18, 293–311.
Ray, J.S., 2009. Radiogenic isotopic ratio variations in carbonatites and associated alkaline silicate rocks: role of crustal assimilation. J. Petrol. 50, 1955–1971.
Rogers, J.J.W., Santosh, M., 2002. Configuration of Columbia, a Mesoproterozoic supercontinent. Gondwana Res. 5, 5–22.
Rogers, J.J.W., Santosh, M., 2009. Tectonics and surface effects of the supercontinent Columbia. Gondwana Res. 15, 373–380.
Rudnick, R.L., Fountain, D.M., 1995. Nature and composition of the continental crust: a lower perspective. Rev. Geophys. 33 (3), 267–310.
Rudnick, R.L., Gao, S., 2003. Composition of the continental crust. In: Holland, H.D., Turekin, K.K. (Eds.), Treatise on Geochemistry. Elsevier, Holland, pp. 1–64.
Santosh, M., 2010. Assembling North China Craton within the Columbia supercontinent: the role of double-sided subduction. Precambrian Res. 178, 149–167.
Santosh, M., Sajeev, K., Li, J.H., 2006. Extreme crustal metamorphism during Columbia supercontinent assembly: evidence from North China Craton. Gondwana Res. 10, 256–266.
Santosh, M., Wilde, S., Li, J.H., 2007. Timing of Paleoproterozoic ultra high temperature metamorphism in the North China Craton: evidence from SHRIMP U–Pb zircon geochronology. Precambrian Res. 159, 178–196.
Santosh, M., Maruyama, S., Yamamoto, S., 2009. The making and breaking of supercontinents: some speculations based on superplumes, superdown welling and the role of tectosphere. Gondwana Res. 15, 324–341.
Santosh, M., Liu, S.J., Tsunogae, T., Li, J.H., 2012. Paleoproterozoic ultrahigh-temperature granulites in the North China Craton: implications for tectonic models on extreme crustal metamorphism. Precambrian Res. 222–223, 77–106.
Santosh, M., Yang, Q.Y., Shaji, E., Tsunogae, T., Ram Mohan, M., Satyanarayanan, M., 2013a. An exotic Mesoarchean microcontinent: the Coorg Block, southern India. Gondwana Res., http://dx.doi.org/10.1016/j.gr.2013.10.005.
Santosh, M., Liu, D., Shi, Y., Liu, S.J., 2013b. Paleoproterozoic accretionary orogenesis in the North China Craton: a SHRIMP zircon study. Precambrian Res. 227, 29–54.
Sawyer, E.W., Cesare, B., Brown, M., 2010. When the continental crust melts. Elements 7, 229–234.
Shang, C.K., Liegeois, J.P., Satir, M., Frisch, W., Nsifa, E.N., 2010. Late Archean high K granite geochronology of the northern metacratonic margin of the Archaean Congro craton, Southern Cameroon: evidence for Pb-loss due to nonmetamorphic causes. Gondwana Res. 18, 337–355.
Shu, L.S., Deng, X.L., Ma, D.S., Xiao, W.J., et al., 2011. Precambrian tectonic evolution of the Tarim Block, NW China: new geochronological insights from the Quruqtagh domain. J. Asian Earth Sci. 42, 774–790.
Smithies, R.H., 2000. The Archaean tonalite–trondhjemite–granodiorite (TTG) series is not an analogue of Cenozoic adakite. Earth Planet Sci. Lett. 182, 115–125.
Smithies, R.H., Champion, D.C., Cassidy, K.F., 2003. Formation of Earth's early Archaean continental crust. Precambrian Res. 127, 89–101.
Smithies, R.H., Champion, D.C., Van Kranendonk, M.J., Howard, H.M., Hickman, A.H., 2005. Modern-style subduction processes in the MesoArchaean: geochemical evidence from the 3.12 Ga Whundo intra-oceanic arc. Earth Planet. Sci. Lett. 231, 221–237.
Smithies, R.H., Van Kranendonk, M.J., Champion, D.C., 2007. The Meso-Archaean emergence of modern-style subduction. Gondwana Res. 11, 50–68.
Stern, C.R., Kilian, R., 1996. Role of the subducted slab, mantle wedge and continental crust in the generation of adakites from the Andean Austral Volcanic Zone. Contrib. Mineral. Petrol. 123, 263–281.
Sylvester, P.J., 1994. Archaean granite plutons. In: Condie, K. (Ed.), Archaean Crustal Evolution. Developments in Precambrian Geology. Elsevier, Amsterdam, pp. 261–314.
Sun, S.S., McDonough, W.F., 1989. Chemical and isotopic systematics of oceanic basalt: implication for mantle composition and Processes. In: Saunders, A.D., Morry, M.J. (Eds.), Magmatism in the ocean basin: Geol Soc. London Spec. Publ., vol. 42, pp. 528–548.
Tate, M.C., Johnson, S.E., 2000. Subvolcanic and deep crustal tonalite genesis beneath the Mexican Peninsular Ranges. J. Geol. 108, 721–728.
Vermeesch, P., 2006. Tectonic discrimination of basalts with classification trees. Geochim. Cosmochim. Acta 70, 1839–1848.
Vavra, G., Schmid, R., Gebauer, D., 1999. Internal morphology, habit and U–Th–Pb microanalysis of amphibole to granulite facies zircon: geochronology of the Ivren Zone (Southern Alps). Contrib. Mineral. Petrol. 134, 380–404.
White, M.J., Kamber, B.S., 2002. On the overabundance of light rare earth elements in terrestrial zircons and its implication for Earth's earliest magmatic differentiation. Earth Planet. Sci. Lett. 204, 333–346.
Whalen, J.B., Percival, J.A., McNicoll, V., Longstafffe, F.J., 2002. A mainly crustal origin for tonalitic granitoid rocks, Superior Province, Canada: implications for Late Archean tectonomagmatic processes. J. Petrol. 43, 1551–1570.
Winchester, J.A., Floyd, P.A., 1976. Geochemical magma type discrimination: application to altered and metamorphosed igneous rocks. Earth Planet. Sci. Lett. 28, 459–469.
Winchester, J.A., Floyd, P.A., 1977. Geochemical discrimination of different magma series and their differentiation products using immobile elements. Chem. Geol. 20, 325–343.
Wang, Q., Zhao, Z.H., Bao, Z.W., Xu, J.F., Liu, W., Li, C.F., 2004. Geochemistry and petrogenesis of the Tongshankou and Yinzu adaktic intrusive rocks and the associated porphyry copper molybdenum mineralization in southeast Hubei, east China. Resour. Geol. 54, 137–152.
Wang, Q., Xu, J.F., Jian, P., Bao, Z.W., Zhao, Z.H., Li, C.F., Xiong, X.L., Ma, J.L., 2006. Petrogenesis of adaktic porphyries in an extensional tectonic setting, Dexing, south China: implications for the genesis of porphyry copper mineralization. J. Petrol. 47, 124–231.
Wolde, B., Gore-Gambella Geotravers, Team., 1996. Tonalite–trondhjemite–granite genesis by partial melting of newly underplated basaltic crust: an example from the Neoproterozoic Birbir magmatic arc, western Ethiopia. Precambrian Res. 76, 3–14.
Xinjiang Bureau of Geology Mineral Resources (BGMR), 1993. Regional Geology of Xinjiang Uygur Autonomous Region. Geological Publishing House, Beijing, pp. 8–33 (in Chinese).
Xiong, X.L., Xia, B., Xu, J.F., Niu, H.C., Xiao, W.S., 2006. Na depletion in modern adakites via melt/rock reaction within the sub-arc mantle. Chem. Geol. 229, 273–292.
Xiong, Q., Zheng, J.P., Yu, C.M., Su, Y.P., Tang, H.Y., Zhang, Z.H., 2009. Zircon U–Pb age and Hf isotope of Quanyishang A-type granite in Yichang: signification for the Yangtze continental cratonization in Paleoproterozoic. Chin. Sci. Bull. 54, 436–446.
Xu, B., Jiang, P., Zheng, H.F., Zou, H.B., Zhang, L.F., Liu, D.Y., 2005. U–Pb zircon geochronology of Neoproterozoic volcanic rocks in the Tarim Block of northwest China: implications for the breakup of Rodinia supercontinent and Neoproterozoic glaciations. Precambrian Res. 136, 107–123.
Xu, B., Xiao, S.H., Zou, H.B., Chen, Y., Li, Z.X., Song, B., Liu, D.Y., Zhou, C.M., Yuan, X.L., 2009. SHRIMP zircon U–Pb age constraints on Neoproterozoic Quruqtagh diamictites in NW China. Precambrian Res. 168, 247–258.
Xu, J.F., Shinjo, R., Defant, M.J., Wang, Q., Rapp, R.P., 2002. Origin of Mesozoic adakitic intrusive rocks in the Ningzhen area of east China: partial melting of delaminated lower continental crust? Geology 30, 1111–1114.
Xu, Z.Q., He, B.Z., Zhang, C.L., Zhang, J.X., Wang, Z.M., Cai, Z.H., 2013. Tectonic framework and crustal evolution of the Precambrian basement of the Tarim Block in NW China: new geochronological evidence from deep drilling samples. Precambrian Res. 235, 150–162.
Yogodzinski, G.M., Kay, R.W., Volynets, O.N., Koloskov, A.V., Kay, S.M., 1995. Magnesian andesite in the western Aleutian Komandorsky region: implications for slab melting and processes in the mantle wedge. Geol. Soc. Am. Bull. 107, 505–519.

Yong, W.J., Zhang, L., Hall, M.C., Mukasa, S.B., Essene, E.J., 2013. The $^{40}Ar/^{39}Ar$ and Rb–Sr chronology of the Precambrian Aksu blueschists in western China. J. Asian Earth Sci. 63, 197–205.

Zhai, M.G., Santosh, M., 2011. The Early Precambrian Odyssey of the North China Craton: a synoptic overview. Gondwana Res. 20, 6–25.

Zhang, C.L., Dong, Y.G., Zhao, Y., Guo, K.Y., 2003. Geochemistry of Meso-Proterozoic volcanites in Western Kunlun: evidence for the plate tectonic evolution. Acta Geol. Sin. 77, 237–245.

Zhang, S.B., Zheng, Y.F., Wu, Y.B., Zhao, Z.F., Gao, S., Wu, F.Y., 2006a. Zircon U–Pb age and Hf–O isotope evidence for Paleoproterozoic metamorphic event in South China. Precambrian Res. 151, 265–288.

Zhang, S.B., Zheng, Y.F., Wu, Y.B., Zhao, Z.F., Gao, S., Wu, F.Y., 2006b. Zircon U–Pb age and Hf isotope evidence for 3.8 Ga crustal remnant and episodic reworking of Archean crust in South China. Earth Planet. Sci. Lett. 252, 56–71.

Zhang, C.L., Li, X.H., Li, Z.X., Lu, S.N., Ye, H.M., Li, H.M., 2007a. Neoproterozoic ultramafic–mafic–carbonatite complex and granitoids in Quruqtagh of northeastern Tarim Block, western China: geochronology, geochemistry and tectonic implications. Precambrian Res. 152, 149–169.

Zhang, C.L., Li, Z.X., Li, X.H., Ye, H.M., 2007b. Early Paleoproterozoic high-K intrusive complex in southwestern Tarim Block NW China: age, geochemistry and implications for the Paleoproterozoic tectonic evolution of Tarim. Gondwana Res. 12, 101–112.

Zhang, C.L., Li, Z.X., Li, X.H., Ye, H.M., 2009. Neoproterozoic mafic dyke swarms in northern margin of the Tarim Block:age, geochemistry and implications on the breakup of Rodinia. J. Asian Earth Sci. 35, 167–179.

Zhang, C.L., Zou, H.B., Wang, H.Y., Li, H.K., Ye, H.M., 2012a. Multiple phases of Neoproterozoic ultramafic–mafic complex in Kuruqtagh, northern margin of Tarim: interaction between plate subduction and mantle plume? Precambrian Res. 222–223, 488–502.

Zhang, C.L., Santosh, M., Li, H.K., Li, Z.X., Zou, H.B., Wang, H.Y., Ye, H.M., 2012b. Precambrian evolution and cratonization of the Tarim Block, NW China: petrology, geochemistry Nd-isotopes and U–Pb zircon geochronology from Archaean gabbro-TTG-potassic granite suite and Paleoproterozoic metamorphic belt. J. Asian Earth Sci. 57, 5–20.

Zhang, H.F., Sun, M., Zhou, X.H., Fan, W.M., Zhai, M.G., Yin, J.F., 2002. Mesozoic lithosphere destruction beneath the North China Craton: evidence from major-, trace-element and Sr–Nd–Pb isotope studies of Fangcheng basalts. Contrib. Mineral. Petrol. 144, 241–253.

Zhang, J., Zhang, C.L., Li, H.K., Ye, X.T., Zhou, H.Y., 2014. Revisit to time and tectonic environment of the Aksu blueschist terrane in northern Tarim, NW China: new evidence from zircon U–Pb age and Hf isotope. Acta Petrol. Sin. (in press).

Zhang, J.X., Yu, S.Y., Gong, J.H., Li, H.K., Hou, K.J., 2013a. The latest Neoarchean–Paleoproterozoic evolution of the Dunhuang block, eastern Tarim craton, northwestern China: evidence from zircon U–Pb dating and Hf isotopic analyses. Precambrian Res. 226, 21–42.

Zhang, C.L., Zou, H.B., Li, H.K., 2013b. Tectonic framework and evolution of the Tarim Block in NW China. Gondwana Res. 23, 1306–1315.

Zhang, H.-F., Zhai, M.-G., Santosh, M., Diwu, C.-R., Li, S.-R., 2011. Geochronology and petrogenesis of Neoarchean potassic meta-granites from Huai'an Complex: implications for the evolution of the North China Craton. Gondwana Res. 20, 82–105.

Zhao, G.C., Cawood, P.A., Wilde, S.A., Sun, M., 2002. Review of global 2.1–1.8 Ga orogens: implications for a pre-Rodinia supercontinent. Earth Sci. Rev. 59, 125–162.

Zhao, G.C., Wilde, S.A., Guo, J.H., Cawood, P.A., Sun, M., Li, X.P., 2010. Single zircon grains record two Paleoproterozoic collisional events in North China Craton. Precambrian Res. 177, 266–276.

Zhao, G.C., Zhai, M.G., 2013. Lithotectonic elements of Precambrian basement in the North China Craton: review and tectonic implications. Gondwana Res. 23, 1207–1240, http://dx.doi.org/10.1016/j.gr.2012.08.016.

Zhao, G.C., Cawood, P.A., Wilde, S.A., Sun, M., Zhang, J., He, Y.H., Yin, C.Q., 2012. Amalgamation of the North China Craton: key issues and discussion. Precambrian Res. 222–223, 55–76.

Zheng, Y.F., Xiao, W.J., Zhao, G.C., 2013. Introduction to tectonics of China. Gondwana Res. 23, 1189–1206.

Zhou, Y.Y., Zhao, T.-P., Wang, C.-Y., Hu, G.-H., 2011. Geochronology and geochemistry of 2.5 to 2.4 Ga granitic plutons from the southern margin of the North China Craton: implications for a tectonic transition from arc to post-collisional setting. Gondwana Res. 20, 171–183.

Zou, H.B., Zindler, A., 1996. Constraints on the degree of dynamic partial melting and source composition using concentration ratios in magmas. Geochim. Cosmochim. Acta 60, 711–717.

Zou, H.B., 1998. Trace element fractionation during modal and nonmodal dynamic melting and open-system melting: a mathematical treatment. Geochim. Cosmochim. Acta 62, 1937–1945.

Zou, H.B., Reid, M.R., 2001. Quantitative modeling of trace element fractionation during incongruent dynamic melting. Geochim. Cosmochim. Acta 65, 153–162.

Zou, H.B., Zindler, A., Xu, X.S., Qi, Q., 2000. Major and trace element, and Nd–Sr–Pb isotope studies of Cenozoic basalts in SE China: mantle sources, regional variations, and tectonic significance. Chem. Geol. 171, 33–47.